

Christopher Albert, BSc

Vibro-acoustic coupling of structural, porous and fluid domains based on simulation and experiment

MASTERARBEIT

zur Erlangung des akademischen Grades
Diplom-Ingenieur

Masterstudium Technische Physik



Technische Universität Graz

Betreuer:

Univ.-Prof. Dipl.-Phys. Dr.rer.nat. Wolfgang von der Linden

Institut für Theoretische Physik – Computational Physics

in Kooperation mit dem

Kompetenzzentrum - Das virtuelle Fahrzeug, Forschungsgesellschaft mbH

Graz, August 2012

Deutsche Fassung:
Beschluss der Curricula-Kommission für Bachelor-, Master- und Diplomstudien vom 10.11.2008
Genehmigung des Senates am 1.12.2008

EIDESSTÄTTLICHE ERKLÄRUNG

Ich erkläre an Eides statt, dass ich die vorliegende Arbeit selbstständig verfasst, andere als die angegebenen Quellen/Hilfsmittel nicht benutzt, und die den benutzten Quellen wörtlich und inhaltlich entnommenen Stellen als solche kenntlich gemacht habe.

Graz, am

.....
(Unterschrift)

Englische Fassung:

STATUTORY DECLARATION

I declare that I have authored this thesis independently, that I have not used other than the declared sources / resources, and that I have explicitly marked all material which has been quoted either literally or by content from the used sources.

.....
date

.....
(signature)

List of Symbols

Symbol	Explanation
$\mathbf{a} := [a_i]$	Bold / lowercase: vector
$\mathbf{A} := [A_{ij}]$	Bold / uppercase: matrix
\mathbb{I}	Identity matrix
$\tilde{f}(\omega) = \frac{1}{\sqrt{2\pi}} \int_{-\infty}^{\infty} f(t)e^{-i\omega t} dt$	Fourier transformation (1-dim.)
$f(t) = \frac{1}{\sqrt{2\pi}} \int_{-\infty}^{\infty} \tilde{f}(\omega)e^{i\omega t} d\omega$	
$\tilde{f}(\mathbf{k}) = \frac{1}{(2\pi)^{3/2}} \int_V f(\mathbf{x})e^{-i\mathbf{k}\cdot\mathbf{x}} d^3\mathbf{x}$	Fourier transformation (3-dim.)
$f(\mathbf{x}) = \frac{1}{(2\pi)^{3/2}} \int_V \tilde{f}(\mathbf{k})e^{i\mathbf{k}\cdot\mathbf{x}} d^3\mathbf{k}$	
$\int_V \delta(\mathbf{x})f(\mathbf{x}) := f(\mathbf{0})$	Delta distribution $\delta(\mathbf{x})$
$a_i^{S_j}$	Quantity defined on surface patch j of domain i
E	Young's modulus
ν	Poisson's ratio
$K = \frac{E}{3(1-2\nu)}$	Bulk modulus
$G = \frac{E}{2(1+\nu)}$	Shear modulus
$\rho_0 \approx 1.2 \text{ kg m}^{-3}$	Density of air at standard conditions ($T = 20^\circ\text{C}$, $p = 101.325 \text{ kPa}$)
$c_0 \approx 343 \text{ m s}^{-1}$	Speed of Sound in air at standard conditions
$Z_0 \approx 412 \text{ N s m}^{-3}$	Characteristic impedance of air at standard conditions
$L_q [\text{dB}] = 20 \log_{10}(q)$	dB scale of a quantity q (Reference value: 1)

Abstract

In this thesis, a method for the prediction of vibro-acoustic system responses based on component characterization is developed. Each subsystem is described by an impedance relation on its surface that can be obtained either experimentally on material samples or from numeric simulations. The method is analyzed and applied to a simplified test case of a rigid air cavity baffled by a flexible plate that is treated with an absorptive porous layer. Possible ways of component characterizations by measurements are proposed. Finally, a comparison between the predicted responses and the results of reference measurements on the assembled physical system is presented.

Contents

Introduction	4
1 Linear Vibroacoustics	6
1.1 Discrete mechanics	6
1.2 Linear acoustics	7
1.3 Linear elastodynamics	9
1.4 Thin plate dynamics	10
1.5 Porous materials	12
1.6 Green's functions	13
1.6.1 Derivation of Green's functions	13
1.6.2 Modal superposition	13
2 Coupling of Subdomains	15
2.1 Surface impedances in 1D	15
2.2 Boundary value problems in 3D	16
2.3 Averaging over patches	17
2.3.1 Condensed transfer functions	18
2.4 Coupling procedure	18
2.4.1 Coupling two fluid domains	19
2.4.2 Coupling an elastic plate and a fluid domain	20
2.4.3 Coupling an elastic plate with two fluid layers	21
2.5 Characterization of subsystems	22
2.5.1 Direct method	22
2.5.2 Indirect method	22
2.6 Numerical results	23
2.6.1 Coupling two acoustic domains	24
3 Test Case and Numerical Models	26
3.1 Test rig parameters	26
3.2 Air cavity	27

3.2.1	Numerical model: Modal superposition	27
3.2.2	Numerical model: Finite element method	29
3.3	Backing plate	29
3.3.1	Numerical model	29
3.4	Porous layer	29
4	Experimental Subsystem Characterization	32
4.1	Structural surface mobility	32
4.1.1	Influence of the environment	36
4.2	Fluids and porous materials	36
4.2.1	Indirect method	37
4.2.2	Simplifications	38
4.2.3	Measurements and results	40
5	Limitations of the Method	44
5.1	Conceptual analysis of averaging errors	44
5.2	Limitations due to the patch size	47
6	Results for the Assembled System	49
6.1	Bare plate + cavity	49
6.2	Bare plate + two cavities	52
6.3	Plate + foam + cavity	53
	Conclusion and Outlook	57
A	Mathematical Background	58
A.1	Elliptic Boundary value problems of second order	58
A.1.1	Weak form and variational formulation	58
A.1.2	Numerical solution using the finite element method	59
A.1.3	Schur complement system	60

Introduction

The accurate prediction of the response of vibro-acoustic systems is of great importance in many areas reaching from basic research in nanoscale systems over ultrasound technology to application in industrial development, building physics and environmental noise protection.

Numerical simulation plays a crucial role in this area, since it is often not possible to predict the behavior of the system in a straightforward way. Furthermore, it enables the optimization of parameters where experimental trial and error is impossible or too costly. Unfortunately, with increasing system complexity, the calculations become more time-consuming and yield less accurate results.

In particular, multilayered systems of poroelastic materials that are commonly used in acoustic treatments pose a special challenge. While it is easy to make rough estimates on their noise-reducing effects, it is difficult to predict their exact behavior numerically. An important reason for this lies in uncertainties in the material parameters due to the manufacturing process.

State of the art

For vibro-acoustic simulations in the low-frequency range, deterministic methods like the Finite Element [Zienkiewicz and Taylor, 2000] and Boundary Element methods [Ciskowski and Brebbia, 1991] are widely used to solve the underlying time harmonic elastic equations [Lalor and Pribsch, 2007]. These numerical methods require elastic parameters, accurate geometrical models and boundary conditions for the calculation domains. They yield accurate results for the spatial distribution of the vibrational and acoustic field quantities for both, structural and fluid domains, up to their frequency limits that are determined by the mesh size. Additionally, they are able to predict the phase relation between time-harmonic quantities. A coupled simulation of structural and fluid domains is possible up to 400 Hz in typical applications (e.g. automotive body structures). For higher frequencies, modeling effort and calculation time limit the practicability.

For predictions in the high frequency range, methods based on the energy flux for reverberant systems (SEA, [Lyon, 1975]) and geometrical propagation models for damped systems (Ray tracing, [Krokstad et al., 1968]) are often used. The results of SEA do not depend on the domain geometry and contain no modal behavior. Without additional experimental data, the predictions can be very inaccurate due to parameter uncertainties. In contrast to that, ray tracing methods take the shape of the calculation domain into account but neglect the wave nature of acoustic fields. Therefore they are only suited for large domains at high frequencies. Neither of the methods is able to reproduce phase relations or diffraction phenomena. Moreover, the validity of the approaches and the possible accuracy is not easily predictable [Fahy, 1994, Bork, 2005].

A commonly used model for poro-elastic damping materials is the Biot theory [Biot, 1941, 1956], which has been originally developed for soil mechanics. The Biot

model allows both, structural and acoustic wave propagation, inside a porous material with an elastic skeleton. The model equations can be implemented in a one-dimensional transfer matrix approach [Allard et al., 1986] or a FEM calculation [Atalla et al., 1998]. It is possible to include Biot model calculations into existing deterministic structure-fluid models and perform a fully coupled simulation. Also general parameters like absorption coefficients can be obtained from the Biot model and used in high-frequency models.

The biggest disadvantage of the Biot model for complex materials is the required amount of parameters [Panneton and Olny, 2006]. In a multi-layer system each layer has to be characterized separately in a series of experiments. For industrially produced materials, the interaction between glued layers is difficult to model.

Aim of this thesis

The method that is proposed in this thesis is based on the principles of deterministic calculations and includes phase information for all considered quantities.

In the assembly of a vibro-acoustic system some parts often already exist physically. If their properties do not change during the assembly it is unnecessary to create numerical models for their description - direct measurements on the subsystems should yield more accurate results. A prediction method for assembled systems should allow for the combination of these data with numerically simulated components.

Therefore a hybrid method is proposed: Instead of a numeric calculation based on material parameters, the vibro-acoustic surface response of a subsystem can be obtained on a real material sample. The method is, however, also compatible with numerical models, therefore it is also applicable to purely simulated subsystems.

Based on a characterization on the boundaries, the procedure is able to assemble a full system from experimentally characterized and numerically modeled subsystems. This allows a choice of the most appropriate characterization method for each component that is independent from the remaining ones.

Acknowledgements

I would like to express my gratitude to Eugène Nijman (Scientific head of NVH and Friction, Virtual Vehicle Competence Center) for his great scientific and personal support during my work. Further thanks go to Giorgio Veronesi (Virtual Vehicle Competence Center) for the good collaboration and the experimental characterization data. I am indebted to my family and my friends who have always supported me during my studies.

Christopher Albert, August 2012

Chapter 1

Linear Vibroacoustics

1.1 Discrete mechanics

A common model for coupled dynamical systems of mechanical bodies is the concept of mass, springs and dampers. In the one-dimensional case, these components react to a displacement $u(t)$ with dynamic forces

$$\begin{aligned} F_{\text{spring}}(t) &= Ku(t) \\ F_{\text{damper}}(t) &= D\dot{u}(t) \\ F_{\text{mass}}(t) &= M\ddot{u}(t), \end{aligned} \tag{1.1}$$

where K , D and M are the spring constant, damping constant and mass, respectively. When a point mass is connected to a rigid anchor by a parallel system of a spring and a damper (Figure 1.1), the overall reaction force is therefore given by

$$F(t) = F_{\text{spring}}(t) + F_{\text{damper}}(t) + F_{\text{mass}}(t) = M\ddot{u}(t) + D\dot{u}(t) + Ku(t).$$

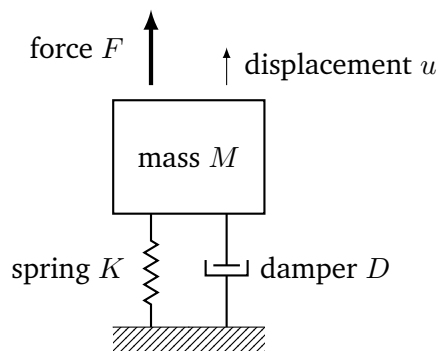


Figure 1.1: System of a mass, a spring and a damper

In the frequency domain, the derivatives are transformed to factors of $i\omega$ and the equation becomes

$$F = (-\omega^2 M + i\omega D + K) u. \tag{1.2}$$

Consequently, the frequency responses of the displacement u , the velocity $v = i\omega u$ and the acceleration $a = -\omega^2 u$ to a force F are

$$\frac{u}{F} = \frac{1}{-\omega^2 M + i\omega D + K} \quad (1.3)$$

$$\frac{v}{F} = \frac{1}{i\omega M + D + K/i\omega} \quad (1.4)$$

$$\frac{a}{F} = \frac{1}{M + D/i\omega - K/\omega^2}, \quad (1.5)$$

respectively.

This concept can be extended to coupled multi-body-systems: Here, the one dimensional displacement u and force F are replaced by vectors of generalized coordinates for all degrees of freedom, \mathbf{u} and \mathbf{f} . The scalar factors K , D and M become matrices \mathbf{K} , \mathbf{D} and \mathbf{M} . Their diagonal elements describe local quantities and the off-diagonal elements quantify the coupling strength. For distributed masses (rigid-body-systems), also the mass matrix will contain off-diagonal terms. The system of equations corresponding to (1.2) is

$$\mathbf{f} = (-\omega^2 \mathbf{M} + i\omega \mathbf{D} + \mathbf{K}) \mathbf{u}. \quad (1.6)$$

Note, that only the variables \mathbf{f} and \mathbf{u} are frequency dependent in this model. In the more general case, the linear factor is replaced by a frequency-dependent dynamic stiffness $\mathbf{K}_{\text{dyn}}(\omega)$ with

$$\mathbf{f} = \mathbf{K}_{\text{dyn}} \mathbf{u}. \quad (1.7)$$

This relation can be used to characterize an arbitrary discrete linear mechanical system in the frequency domain. We have to keep in mind, that all discrete approximations for continuous vibro-acoustic problems can be interpreted as a discrete network of masses, springs and dampers.

1.2 Linear acoustics

The theory of linear acoustics describes the relationship of a pressure field and a corresponding velocity field in every point of a region in space.

The wave-like behavior of the pressure and velocity fields can be derived from fluid mechanics. For a non-viscous fluid model we use the continuity equation for the density ρ and the flow velocity \mathbf{v} ,

$$\frac{\partial \rho}{\partial t} + \nabla \cdot (\rho \mathbf{v}) = \frac{\partial m}{\partial t}. \quad (1.8)$$

The right side is a source term that describes an externally introduced mass density fluctuation. Newton's second law of motion yields a momentum change due to the

pressure gradient,

$$\rho \left(\frac{\partial \mathbf{v}}{\partial t} + (\mathbf{v} \cdot \nabla) \mathbf{v} \right) + \nabla p = 0. \quad (1.9)$$

These equations are the Euler equations [Landau and Lifshitz, 1987]¹, which contain quadratic velocity terms and are thus nonlinear in general. In acoustics, a small perturbation from equilibrium ($\rho_0 + \rho(\mathbf{x}, t)$, $p_0 + p(\mathbf{x}, t)$, $\mathbf{v}_0 + \mathbf{v}(\mathbf{x}, t)$) is assumed. The zeroth-order terms do not depend on space or time. If we neglect quadratic and higher terms of the perturbation terms, (1.8) and (1.9) can be simplified to

$$\frac{\partial \rho}{\partial t} + \rho_0 \nabla \cdot \mathbf{v} = \frac{\partial m}{\partial t} \quad (1.10)$$

$$\rho_0 \frac{\partial \mathbf{v}}{\partial t} + \nabla p = 0. \quad (1.11)$$

If we assume adiabatic conditions and near equilibrium, the thermodynamic equations of state yield a linear relationship between p and ρ ,

$$\frac{\partial p}{\partial \rho} = c^2$$

We apply a time derivative to (1.10) and a ∇ -operator to (1.11) to eliminate \mathbf{v} and obtain

$$\Delta p - \frac{1}{c^2} \frac{\partial^2 p}{\partial t^2} = -\rho_0 \frac{\partial q}{\partial t} \quad (1.12)$$

$q = \frac{1}{\rho_0} \frac{\partial m}{\partial t}$ is the volumetric flow rate of mass density ρ_0 that is introduced by sound sources. Damping in the system can be modeled as in (1.1) by introducing an equivalent damping factor ε on a first time derivative of the pressure and the damped version of (1.12) is written as

$$\Delta p - 2 \frac{\varepsilon}{c^2} \frac{\partial p}{\partial t} - \frac{1}{c^2} \frac{\partial^2 p}{\partial t^2} = -\rho_0 \frac{\partial q}{\partial t} \quad (1.13)$$

By transformation to the frequency domain, the equation is transformed into the damped acoustic Helmholtz equation,

$$\Delta p - 2i\varepsilon \frac{\omega}{c^2} p + \frac{\omega^2}{c^2} p = -i\omega \rho_0 q \quad (1.14)$$

with the wave number $k = \frac{\omega}{c}$. The wavelength $\lambda = \frac{2\pi}{k}$ becomes shorter as the frequency increases, which is shown in Figure 1.2.

¹More generally, the right side of the second equation contains also external forces that lead to dipole sound sources [Fahy, 2001]. We are only considering monopole sources here, so it is assumed to be zero.

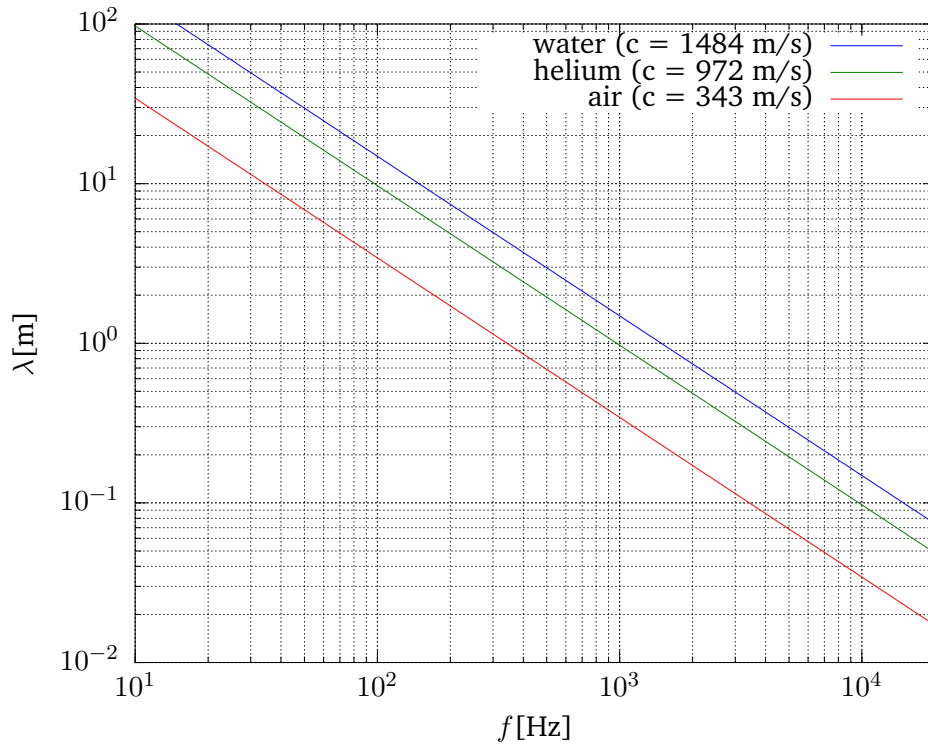


Figure 1.2: Acoustic wavelengths in media with different speed of sound

Pressure and particle velocity in the fluid are related by (1.10) and (1.11),

$$\nabla \cdot \mathbf{v} = -i\omega \frac{1}{c^2 \rho_0} p = -i \frac{k}{Z_c} p \quad (1.15)$$

$$\nabla p = -i\omega \rho_0 \mathbf{v} = -ik Z_c \mathbf{v}. \quad (1.16)$$

$Z_c = \rho_0 c$ is the characteristic impedance of the fluid.

1.3 Linear elastodynamics

In elastic solids, also shear forces play a role, opposed to fluids, where only compression is relevant. Therefore, instead of the pressure p , the forces onto an infinitesimal volume of the solid are expressed by a stress tensor σ_{ij} , whose diagonal Cartesian components describe pressures in the three space directions. The off-diagonal elements describe shear forces in direction i , applied to the normal face in direction j . Traditionally, the displacements \mathbf{u} are used to describe the solid motion instead of the velocities $\mathbf{v} = \frac{\partial \mathbf{u}}{\partial t}$.

For small perturbations from equilibrium, the equations of motion become linear as in 1.2. For isotropic elastic solids, the relationship between stresses and displacements can be derived using fundamental spring constants K (bulk modulus) and G (shear modulus). According to Landau and Lifshitz [1986], the stress-strain relation

is given by

$$\sigma_{ij} = \delta_{ij} \left(K - \frac{2}{3}G \right) \nabla \cdot \mathbf{u} + G \left(\frac{\partial u_i}{\partial x_j} + \frac{\partial u_j}{\partial x_i} \right). \quad (1.17)$$

Using the balance of dynamic forces (in analogy to 1.11),

$$\nabla \cdot \sigma_{ij} = \rho \frac{\partial^2 \mathbf{u}}{\partial t^2} + \mathbf{f}_{ext},$$

the elastic wave equations in the time domain are given by

$$G\Delta \mathbf{u} + \left(K - \frac{2}{3}G \right) \nabla \cdot (\nabla \cdot \mathbf{u}) = \rho \frac{\partial^2 \mathbf{u}}{\partial t^2} + \mathbf{f}_{ext}$$

and in the frequency domain by

$$G\Delta \mathbf{u} + \left(K - \frac{2}{3}G \right) \nabla \cdot (\nabla \cdot \mathbf{u}) + \rho \omega^2 \mathbf{u} = \mathbf{f}_{ext}. \quad (1.18)$$

There are now two types of waves with different wave numbers:

- Longitudinal waves with

$$c_l = \sqrt{\frac{K + 4G/3}{\rho}}$$

- Transversal waves with

$$c_t = \sqrt{\frac{G}{\rho}}$$

Using this notation, the Eigenvalue problem for (1.18) without excitation forces can be written as

$$c_t^2 \Delta \mathbf{u} + (c_l^2 - c_t^2) \nabla \cdot (\nabla \cdot \mathbf{u}) + \omega^2 \mathbf{u} = 0,$$

where $\mathbf{u} = \mathbf{u}_l + \mathbf{u}_t$ is a combination of longitudinal and transversal displacement that satisfy

$$\Delta \mathbf{u}_l + \frac{\omega^2}{c_l^2} \mathbf{u}_l = 0, \quad \Delta \mathbf{u}_t + \frac{\omega^2}{c_t^2} \mathbf{u}_t = 0.$$

1.4 Thin plate dynamics

A plate with a small thickness h in z -direction is extremely stiff to compression but able to bend away from its equilibrium plane. Therefore, the elastic equations can be simplified to describe just the bending motion and neglect the in-plane motion. Landau and Lifshitz [1986] give a derivation of this thin-plate model commonly known as the Kirchhoff-Love plate. The model assumptions are the following:

- The displacement components parallel to the xy -plane, u_x and u_y , can be neglected if the bending is small enough. The remaining quantity is the out-of-plane displacement $u_z =: u$.
- External forces result in bending motion with large in-plane stresses. Therefore the out-of-plane stresses σ_{xz} , σ_{yz} , σ_{zz} can be neglected.

Several transformations of the original elastic equations (1.17) results in the balance of forces in the z direction,

$$D\Delta^2 u - f = 0$$

where the plate bending stiffness D is given by

$$D = \frac{Eh^3}{12(1-\nu^2)}.$$

In the dynamic case, the out-of-plane force f is given by the inertia and the external forces f_{ext} ,

$$f = \rho \cdot h \cdot \frac{\partial^2 u}{\partial t^2} + f_{ext}.$$

In the frequency domain, we obtain the fourth-order equivalent to (1.14),

$$D\Delta^2 u + \rho h \omega^2 u = f_{ext}.$$

The relationship between k and ω is no more linear, the dispersion relation is given by

$$k = \sqrt[4]{\frac{\rho h}{D}} \sqrt{\omega}$$

which leads to a frequency-dependent wave propagation speed,

$$c(\omega) = \sqrt[4]{\frac{D}{\rho h}} \sqrt{\omega}.$$

In comparison to fluids (Figure 1.2), the wavelength in plates (Figure 1.3) decreases only with the square root of the frequency. When a plate is radiating into a fluid, the wavelength of the compression wave and the bending wave matches at some point. For this so-called coincidence frequency the radiation efficiency reaches its maximum. The relevant frequencies for this work are below the coincidence frequency, which is ≈ 6000 Hz with a wavelength of 5.6 cm for a 2 mm steel plate in air.

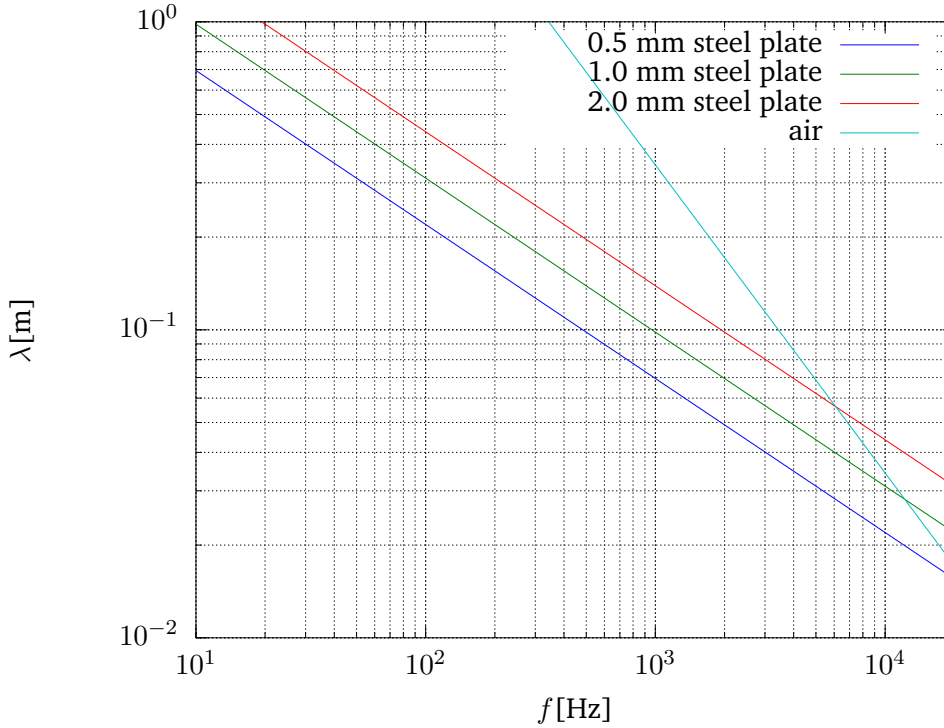


Figure 1.3: Bending wavelength for steel plates of different thickness and coincidence with acoustic waves in air

1.5 Porous materials

A phenomenological model based on statistical analysis of fibrous materials has been proposed by Delany and Bazley [1970]. Here, the model for a poroelastic material is an equivalent fluid with characteristic impedance and complex wave number

$$Z_c = \rho_0 c_0 (1 + 0.057 X^{-0.754} - i 0.087 X^{-0.732}) \quad (1.19)$$

$$k = \frac{\omega}{c_0} (1 + 0.0978 X^{-0.700} - i 0.189 X^{-0.595}) . \quad (1.20)$$

The quantity $X = \frac{\rho_0 f}{\sigma}$ depends only on the fluid parameters and the flow resistivity σ . The coefficients and exponents have been obtained by a linear regression of experimental data for a multitude of samples with different σ . Allard and Atalla [2009] state that the predictions by this model will have the correct order of magnitude for $0.01 < X < 1$.

More complex models take microscopic parameters into account. Pride et al. [1993] give a detailed derivation of a model for the drag forces in variable-width flow channels. By asymptotic analysis for the low- and high-frequency domain and interpolating over the mid-frequency region, the frequency-dependent effective density and stiffness of the fluid can be derived.

Since the equivalent fluid of Delany and Bazley [1970] yields very good agreement with measurements for the materials investigated in this work, it is not necessary to

discuss more complicated models in this context.

1.6 Green's functions

1.6.1 Derivation of Green's functions

The definition of a Green's function $G(\mathbf{r}, \mathbf{r}')$ is usually given as a function that satisfies a partial differential equation with a point source.

For of the Helmholtz equation (1.14), $G(\mathbf{r}, \mathbf{r}')$ it is given by

$$\Delta G(\mathbf{r}, \mathbf{r}') - 2i\varepsilon \frac{\omega}{c^2} G(\mathbf{r}, \mathbf{r}') + \frac{\omega^2}{c^2} G(\mathbf{r}, \mathbf{r}') = -i\omega\rho\delta(\mathbf{r} - \mathbf{r}'). \quad (1.21)$$

Let us consider a solution G for the point-excitation case and an unknown solution p . We apply the identity

$$\nabla(f\nabla g) = \nabla f \cdot \nabla g - f\Delta g,$$

to obtain

$$\begin{aligned} \nabla(G\nabla p) - \nabla(p\nabla G) &= p\Delta G - G\Delta p \\ &= -i\omega\rho(\delta(\mathbf{r} - \mathbf{r}')p - qG). \end{aligned}$$

Integration and application of the divergence theorem yields an expression for the solution,

$$p(\mathbf{r}) = \frac{i}{\omega\rho} \int_{\partial\Omega} \left(G(\mathbf{r}, \mathbf{r}') \frac{\partial p(\mathbf{r}')}{\partial n} - \frac{\partial G(\mathbf{r}, \mathbf{r}')}{\partial n} p(\mathbf{r}') \right) dS' + \int_{\Omega} G(\mathbf{r}, \mathbf{r}') q(\mathbf{r}') dV. \quad (1.22)$$

Since the normal derivative of p is proportional to the particle velocity v (1.16), we can also write

$$p(\mathbf{r}) = \int_{\partial\Omega} \left(G(\mathbf{r}, \mathbf{r}') v_n(\mathbf{r}') - \frac{i}{\omega\rho} \frac{\partial G(\mathbf{r}, \mathbf{r}')}{\partial n} p(\mathbf{r}') \right) dS' + \int_{\Omega} G(\mathbf{r}, \mathbf{r}') q(\mathbf{r}') dV,$$

where $v_n(\mathbf{r}')$ is the normal velocity on the boundary.

1.6.2 Modal superposition

To find a solution for $G(\mathbf{r}, \mathbf{r}')$, we will first consider the homogenous problem of (1.14) ($q = 0$). Here, the equation becomes an eigenvalue problem at frequency ω_i ,

$$\Delta p(\mathbf{r}) + \frac{\omega_i^2}{c^2} p(\mathbf{r}) = 0. \quad (1.23)$$

A solution of (1.23) is called a *mode* $\phi_i(\mathbf{r})$ of the system. If there is no damping inside the system, there will be a singularity in the solution for an excitation with

the eigenfrequency ω_i of the mode. It can be shown [Polyanin, 2002], that any sufficiently regular function compatible with the boundary conditions can be written as a superposition of modes,

$$f(\mathbf{r}) = \sum_i f_i \phi_i(\mathbf{r}). \quad (1.24)$$

Furthermore, the modes fulfill an orthogonality relation

$$\int_{\Omega} \phi_i(\mathbf{r}) \phi_j(\mathbf{r}) dV = \delta_{ij} \quad (1.25)$$

In the physical sense this means, that all time-harmonic movements of an arbitrarily excited elastic system can be represented by the stationary vibration modes of the system without excitations - for example the harmonics of a string.

For the Green's function we use the ansatz

$$G(\mathbf{r}, \mathbf{r}') = \sum_{i,j} g_{ij} \phi_i(\mathbf{r}) \phi_j(\mathbf{r}').$$

Using the orthogonality (1.25) we multiply (1.21) by the mode $\phi_i(\mathbf{r}')$ and integrate over \mathbf{r}' to obtain

$$g_{ii} \left(-\frac{\omega_i^2}{c^2} \phi_i(\mathbf{r}) - 2i\varepsilon \frac{\omega}{c^2} \phi_i(\mathbf{r}) + \frac{\omega^2}{c^2} \phi_i(\mathbf{r}) \right) = -i\omega\rho\phi_i(\mathbf{r}).$$

Consequently,

$$g_{ii} = \frac{i\omega\rho c^2}{\omega_i^2 - \omega^2 + 2i\varepsilon\omega},$$

$$g_{ij} = 0 \text{ for } i \neq j.$$

The Green's function can thus be derived by finding the modes of the equation and summing up the contributions between excitation at \mathbf{r}' and receiving position \mathbf{r} . In numeric calculations, we will have to truncate the series above the maximum frequency of interest ω_{\max} . An obvious consequence of the modal summation is the reciprocity of Green's functions:

$$G(\mathbf{r}, \mathbf{r}') = G(\mathbf{r}', \mathbf{r}) \quad (1.26)$$

Chapter 2

Coupling of Subdomains

With the knowledge of the mathematical formulation of vibro-acoustic systems we are now going to couple different domains. The coupling method should allow both experimental and numerical characterization of subdomains. Since the information on the boundary should be sufficient and placing sensors inside a domain is not always possible, a non-overlapping coupling method should be suited best. One example for such a method is the Patch Transfer Function (PTF) approach, which will be used in this thesis. The PTF coupling scheme has been originally introduced as a tool to couple different domains with numerical methods such as the Finite Element Method (A.1.2). It has been proposed by Ouisse et al. [2005], where a review of the method including numerical examples can be found. Examples for applications have been given by Pavic [2010] for acoustic coupling, Aucejo et al. [2010] for a plate-cavity system and Chazot and Guyader [2007] for a multi-layered transmission-loss problem.

The idea of the PTF is, that the coupling behavior of any linear acoustic or elastic system can be characterized solely by a linear relationship on the surface. Each system is described by a surface impedance or mobility, defined on a coarse grid of patches. The aim is to speed up calculation time, while retaining results of acceptable accuracy. In terms of domain decomposition methods, the PTF method is a Schur complement method (A.6). The discretization of the coupling surfaces is coarser than the original FEM grid and the shape functions are of zeroth order (uniform values over one patch).

While the approach was intended for numerical calculations, it is extended by proposals for experimental procedures to obtain the patch transfer functions for the components of a coupled vibro-acoustic system with damping material. The numerically assembled coupled system are validated by reference measurements.

2.1 Surface impedances in 1D

As described in chapter 1, a central feature of vibroacoustics is the response of a system due to a forced excitation. It does not make a difference, if we choose either u , v or a as our movement quantity, since they are proportional in the frequency

domain. As a convention we will use the velocity v as the main variable.

If we move the boundary of a one-dimensional system, it responds with a surface pressure p that depends on the overall characteristics of the system and the frequency. The relation between the quantities p and v on the surface is called the surface impedance and can be written as a linear law,

$$p = Z v . \quad (2.1)$$

The inverse of Z is called the mobility Y .

2.2 Boundary value problems in 3D

Let us now extend the concept of surface impedances from 2.1 to 3-dimensional systems with 2-dimensional surfaces. The solution of homogenous problems for partial differential equations like (1.14) is uniquely given by imposing boundary conditions [Polyanin, 2002]. This can be easily understood in a physical way: If a mechanical system is only excited on its surface, the response in the interior is uniquely given by this excitation. We are going to consider the following cases:

1. Imposed pressure (*Dirichlet* boundary condition):

$$p(\mathbf{x})|_{\mathbf{x} \in S} = p^S(\mathbf{x})$$

2. Imposed normal velocities (*Neumann* boundary condition):

$$\left. \frac{\partial p(\mathbf{x})}{\partial n} \right|_{\mathbf{x} \in S} = i \omega \rho v^S(\mathbf{x})$$

Since we assume a second order equation for $p(\mathbf{x})$, only one of the two boundary conditions can be imposed in a specific position on the boundary. The physical interpretation of this is that there is always a response of the system, so we cannot impose both, a forced surface pressure and velocity, at the same time. The second variable on each point in the domain (including the surface) can be obtained by the relations:

1. Mobility relation for imposed pressures

$$v(\mathbf{x}) = \int_S Y(\mathbf{x}, \mathbf{x}') p^S(\mathbf{x}') dS' . \quad (2.2)$$

2. Impedance relation for imposed velocities

$$p(\mathbf{x}) = \int_S Z(\mathbf{x}, \mathbf{x}') v^S(\mathbf{x}') dS' . \quad (2.3)$$

$Z(x, x')$ and $Y(x, x')$ can be principally derived from the model equations (1.6). If both \mathbf{x} and \mathbf{x}' are on the surface, they are called *surface impedance / mobility*. In

the theory of elliptic partial differential equations they are known as the *Dirichlet-to-Neumann map*, a special case of a Poincaré-Steklov-Operator. In the one-dimensional case, (2.3) reduces again to (2.1).

2.3 Averaging over patches

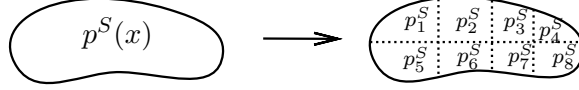


Figure 2.1: Discrete approximation of the surface pressure values $p^S(\mathbf{x})$ by p_i^S

In measurements and simulations, the integrals (2.2) and (2.3) cannot be evaluated exactly. They can be approximated in a straightforward way by splitting the boundary surface into patches and assuming averaged constant values for the quantities over one patch (Figure 2.1),

$$p^S(\mathbf{x})|_{\mathbf{x} \text{ in Patch } i} \approx \frac{1}{S_i} \int_{S_i} p^S(\mathbf{x}) dS =: p_i^S$$

$$v^S(\mathbf{x})|_{\mathbf{x} \text{ in Patch } i} \approx \frac{1}{S_i} \int_{S_i} v^S(\mathbf{x}) dS =: v_i^S.$$

The transfer functions from patch i to position \mathbf{x} are then given by

$$Y_i^T(\mathbf{x}) := \int_{S_i} Y(\mathbf{x}, \mathbf{x}') dS' \quad (2.4)$$

$$Z_i^T(\mathbf{x}) := \int_{S_i} Z(\mathbf{x}, \mathbf{x}') dS' \quad (2.5)$$

and the transfer functions between patches i and j by

$$Y_{ij}^S := \int_{S_i} \int_{S_j} Y(\mathbf{x}, \mathbf{x}') dS' dS \quad (2.6)$$

$$Z_{ij}^S := \int_{S_i} \int_{S_j} Z(\mathbf{x}, \mathbf{x}') dS' dS. \quad (2.7)$$

The integral equations (2.2) and (2.3) on the surface become matrix equations

$$v_i^S = Y_{ij}^S p_j \quad (2.8)$$

$$p_i^S = Z_{ij}^S v_j, \quad (2.9)$$

where the mobility matrix \mathbf{Y}^S is an approximation for the inverse of the impedance matrix \mathbf{Z}^S ,

$$\mathbf{Y}^S \approx (\mathbf{Z}^S)^{-1}. \quad (2.10)$$

The patch values can be obtained by averaging over measured or simulated quanti-

ties inside a patch.¹

2.3.1 Condensed transfer functions

As mentioned in (A.6), the degrees of freedom of a system that are not excited directly can be eliminated in the matrix equation. A physical interpretation of this equation is the lumping together of several masses, springs and dampers in (1.7) to a single "black box" defined by its stiffness matrix between the excitation positions. Firstly, all homogenous systems can be reduced to the surface, which corresponds to (2.2) - (2.9). But even for more complicated boundary conditions, we can go a step further. All sections of the boundary that are neither excited directly nor coupled to a subsystems of interest can be eliminated in the equation. The resulting condensed impedance relation will only include these sections and contain the full information about the system response including the remaining boundary conditions. The following transfer functions will all be of this kind.

2.4 Coupling procedure

In this section, we will use the relations (2.9) and (2.8) to couple systems on their common interface. The approach is based on the superposition principle (See Bobrovnikii [2001] for a detailed analysis): The coupled response of one subsystem is given the sum of two (virtual) configurations. For a fluid subsystem this is

1. The pressure response due to internal sources $\tilde{\mathbf{v}}^A$ if the coupled interface is blocked ($\tilde{\mathbf{v}}^S = \mathbf{0}$).
2. The pressure response due to the (yet unknown) interface velocity \mathbf{v}^S of the coupled system, when the internal sources are switched off.

For a structural subsystem it is given by

1. The velocity response due to internal sources $\tilde{\mathbf{p}}^F$ if the coupled interface is free ($\tilde{\mathbf{p}}^S = \mathbf{0}$).
2. The velocity response due to the (yet unknown) interface pressure \mathbf{p}^S of the coupled system, when the internal sources are switched off.

In the following sections, an internal excitation of one subsystem is assumed to be independent from the other subsystems (no back-action to the source itself), so we denote internal sources by $\mathbf{v}^A \approx \tilde{\mathbf{v}}^A$, $\mathbf{p}^F \approx \tilde{\mathbf{p}}^F$.

¹The approach is however not limited to patches, since (2.8), (2.9) hold for any finite approximation of the boundary values.

2.4.1 Coupling two fluid domains

For an uncoupled system, let \mathbf{Z}_1^S and \mathbf{Z}_2^S be the surface impedances of the two respective domains on their common interface. We introduce velocity sources \mathbf{v}^A in system number 1 and the respective transfer functions \mathbf{Z}^{AS} to the coupling surface. We denote the surface pressures and velocities by \mathbf{p}^S and \mathbf{v}^S . The quantities are then related by the system impedances,

$$\begin{aligned}\mathbf{p}_1^S &= \mathbf{Z}_1^S \mathbf{v}_1^S + \mathbf{Z}_1^{AS} \mathbf{v}_1^A \\ \mathbf{p}_2^S &= \mathbf{Z}_2^S \mathbf{v}_2^S.\end{aligned}$$

$\mathbf{Z}^{AS} \mathbf{v}^A$ are the surface pressures $\tilde{\mathbf{p}}_1^S$ in the first system with a blocked interface ($\tilde{\mathbf{v}}_1^S = 0$) due to the internal sources \mathbf{v}^A .

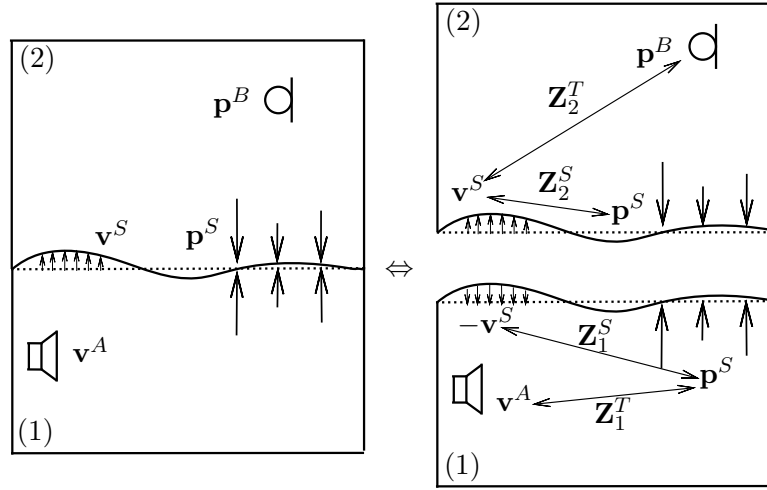


Figure 2.2: Coupled fluid cavities. Pressures \mathbf{p}^S and velocities \mathbf{v}^S on the interface have to match. Source \mathbf{v}^A , Receiver \mathbf{p}^B . Surface/Transfer Impedances: \mathbf{Z}^S , \mathbf{Z}^T

When the two systems are coupled (Fig. 2.2), the pressures and the velocities on the surface have to match on the interface,

$$\begin{aligned}\mathbf{p}^S &= \mathbf{p}_1^S = \mathbf{p}_2^S \\ \mathbf{v}^S &= -\mathbf{v}_1^S = \mathbf{v}_2^S.\end{aligned}$$

In this case, the direction of the normal velocity is defined as pointing into the inside of the domain. The pressures at the coupling surface are given by the relation

$$\mathbf{p}^S = -\mathbf{Z}_1^S \mathbf{v}^S + \mathbf{Z}^{AS} \mathbf{v}^A = \mathbf{Z}_2^S \mathbf{v}^S$$

and we obtain an equation for the surface velocities

$$(\mathbf{Z}_1^S + \mathbf{Z}_2^S) \mathbf{v}^S = -\mathbf{Z}^{AS} \mathbf{v}^A. \quad (2.11)$$

For the receiving pressures \mathbf{p}^B with the corresponding transfer functions \mathbf{Z}^{SB} , we

obtain

$$\mathbf{p}^B = \mathbf{Z}^{SB} \mathbf{v}^S .$$

2.4.2 Coupling an elastic plate and a fluid domain

Let \mathbf{Y} denote the elastic plate mobility and \mathbf{Z}^S the cavity's surface impedance with

$$\mathbf{v}_e = \mathbf{Y} (\mathbf{p}_e^S + \mathbf{p}_e^F) \quad (2.12)$$

$$\mathbf{p}_f^S = \mathbf{Z}^S \mathbf{v}_f^S . \quad (2.13)$$

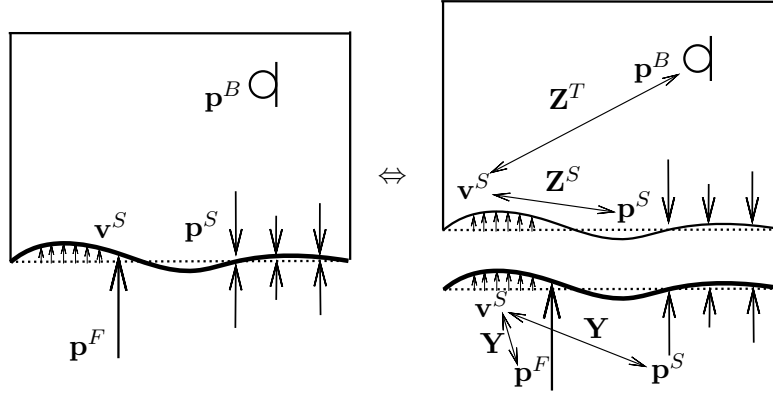


Figure 2.3: Elastic plate coupled to a fluid cavity. Pressures \mathbf{p}^S and velocities \mathbf{v}^S on the interface have to match. Source \mathbf{p}^F , Receiver \mathbf{p}^B . Mobility: \mathbf{Y} . Surface/Transfer Impedances: $\mathbf{Z}^S, \mathbf{Z}^T$

$\mathbf{Y} \mathbf{p}^F = \tilde{\mathbf{v}}_e$ would be the plate's response to the force in vacuo ($\mathbf{p}_e^S = 0$). The continuity conditions for the coupled case (Fig. 2.3) are

$$\begin{aligned} \mathbf{p}^S &= \mathbf{p}_e^S = \mathbf{p}_f^S \\ \mathbf{v}^S &= \mathbf{v}_e^S = \mathbf{v}_f^S . \end{aligned}$$

From (2.13) we obtain

$$\mathbf{p}^S = \mathbf{Z}^S \mathbf{v}^S .$$

The mobility relation (2.12) yields

$$\mathbf{v}^S = \mathbf{Y} (\mathbf{p}^F + \mathbf{p}^S) = \mathbf{Y} (\mathbf{p}^F + \mathbf{Z}^S \mathbf{v}^S) ,$$

which results in

$$(\mathbb{I} - \mathbf{Y} \mathbf{Z}^S) \mathbf{v}^S = \mathbf{Y} \mathbf{p}^F . \quad (2.14)$$

The receiving point pressures are again

$$\mathbf{p}^B = \mathbf{Z}^{SB} \mathbf{v}^S$$

2.4.3 Coupling an elastic plate with two fluid layers

Combining the two coupling cases defined above (fig. 2.4), we can now couple an elastic plate (0) with two acoustic layers (1), (2) with the continuity conditions on two surfaces S_1 and S_2 ,

$$\begin{aligned} \mathbf{p}^{S_0} &= \mathbf{p}_0^{S_0} = \mathbf{p}_1^{S_0} \\ \mathbf{v}^{S_0} &= \mathbf{v}_0^{S_0} = \mathbf{v}_1^{S_0} \\ \mathbf{p}^{S_1} &= \mathbf{p}_1^{S_1} = \mathbf{p}_2^{S_1} \\ \mathbf{v}^{S_1} &= -\mathbf{v}_1^{S_1} = \mathbf{v}_2^{S_1} . \end{aligned}$$

The impedance relations follow as

$$\mathbf{v}^{S_0} = \mathbf{Y} (\mathbf{p}^{S_0} + \mathbf{p}^F) \quad (2.15)$$

$$\mathbf{p}^{S_0} = \mathbf{Z}_1^{S_0} \mathbf{v}^{S_0} - \mathbf{Z}_1^{S_1 S_0} \mathbf{v}^{S_1} \quad (2.16)$$

$$\mathbf{p}^{S_1} = \mathbf{Z}_1^{S_0 S_1} \mathbf{v}^{S_0} - \mathbf{Z}_1^{S_1} \mathbf{v}^{S_1} \quad (2.17)$$

$$\mathbf{p}^{S_1} = \mathbf{Z}_2^{S_1} \mathbf{v}^{S_1} , \quad (2.18)$$

where \mathbf{v}^{S_i} are the velocities on the coupling surface i , \mathbf{p}^{S_i} the surface pressures, \mathbf{p}^F the source term, \mathbf{Y} the plate mobility and $\mathbf{Z}_k^{S_i}$, $\mathbf{Z}_k^{S_i S_j}$ the respective surface and transfer impedances between surfaces i and j in the fluid domain k .

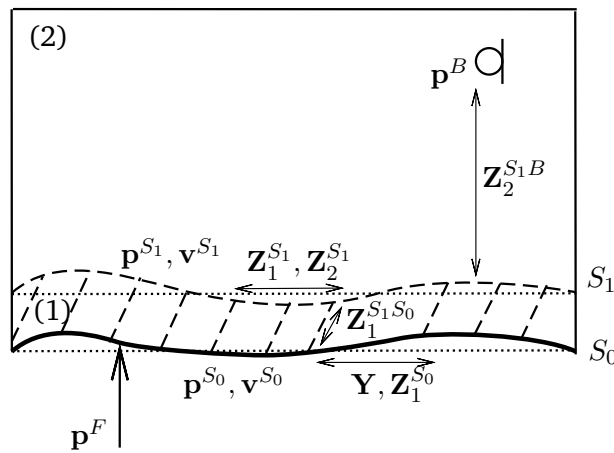


Figure 2.4: Coupled plate-fluid-fluid system. Pressures \mathbf{p}^S and velocities \mathbf{v}^S on the respective interfaces match. Source \mathbf{p}^F , Receiver \mathbf{p}^B

The matrix form reads

$$\begin{pmatrix} \mathbb{I} & -\mathbf{Z}_1^{S_0} & \mathbf{Z}_{1V}^{S_1 S_0} \\ -\mathbf{Y} & \mathbb{I} & 0 \\ 0 & -\mathbf{Z}_1^{S_0 S_1} & \mathbf{Z}_1^{S_1} + \mathbf{Z}_2^{S_1} \end{pmatrix} \begin{pmatrix} \mathbf{p}^{S_0} \\ \mathbf{v}^{S_0} \\ \mathbf{v}^{S_1} \end{pmatrix} = \begin{pmatrix} 0 \\ \mathbf{Y} \mathbf{p}^F \\ 0 \end{pmatrix}.$$

2.5 Characterization of subsystems

2.5.1 Direct method

According to the matrix equations (2.9), (2.8) we can directly obtain the matrix elements of either \mathbf{Z}^S or its inverse \mathbf{Y}^S by the following direct methods:

1. To determine \mathbf{Y}^S , we excite with a surface pressure (force) p_k^S at patch k and leave all the other patches free with $p_{j \neq k}^S = 0$. The i -th row of \mathbf{Y}^S is given by the ratio of all surface velocities v_i^S to the single pressure p_k^S ,

$$Y_{ik}^S = \left. \frac{v_i^S}{p_k^S} \right|_{p_{j \neq k}^S = 0}. \quad (2.19)$$

2. To obtain \mathbf{Z}^S , we excite with a surface velocity v_k^S at a certain patch k and block all other patches so that $v_{j \neq k}^S = 0$. Then the i -th row of \mathbf{Z}^S is given by the ratio of all surface pressures p_i^S to the single velocity v_k^S ,

$$Z_{ik}^S = \left. \frac{p_i^S}{v_k^S} \right|_{v_{j \neq k}^S = 0}. \quad (2.20)$$

The first case will be the natural method for elastic domains, the second one for acoustic domains. In the numerical model, we can just successively apply these boundary conditions and obtain the blocked pressures or free velocities on the surface. In principle this can also be done experimentally, as we will see in the next chapter (4.1).

Another method, that is only possible in the numerical model is the condensation of the stiffness matrix to obtain the Schur complement system (A.1.3) on the boundary. Since detailed information is not needed, the condensed matrix is then interpolated to a coarser patch grid. For large patches, the direct method described above should be significantly faster.

2.5.2 Indirect method

The characterization of subsystems is not limited to the direct reading of the matrix elements. In general, to obtain an accurate values for \mathbf{Y} or \mathbf{Z} on N patches, at least N independent configurations of different \mathbf{p}^S and \mathbf{v}^S have to be found. The impedance or admittance of the system can be reconstructed from (2.9) and (2.8)

by solving the respective inverse problem

$$\begin{pmatrix} p_{11}^S & p_{12}^S & \cdots \\ p_{21}^S & p_{22}^S & \cdots \\ \vdots & \vdots & \ddots \end{pmatrix} = \mathbf{Z} \begin{pmatrix} v_{11}^S & v_{12}^S & \cdots \\ v_{21}^S & v_{22}^S & \cdots \\ \vdots & \vdots & \ddots \end{pmatrix},$$

$$\begin{pmatrix} v_{11}^S & v_{12}^S & \cdots \\ v_{21}^S & v_{22}^S & \cdots \\ \vdots & \vdots & \ddots \end{pmatrix} = \mathbf{Y} \begin{pmatrix} p_{11}^S & p_{12}^S & \cdots \\ p_{21}^S & p_{22}^S & \cdots \\ \vdots & \vdots & \ddots \end{pmatrix}.$$

The columns of the matrices

$$\mathbf{P} := \begin{pmatrix} p_{11}^S & p_{12}^S & \cdots \\ p_{21}^S & p_{22}^S & \cdots \\ \vdots & \vdots & \ddots \end{pmatrix}$$

and

$$\mathbf{V} := \begin{pmatrix} v_{11}^S & v_{12}^S & \cdots \\ v_{21}^S & v_{22}^S & \cdots \\ \vdots & \vdots & \ddots \end{pmatrix}$$

are the vectors of the patch values for each single configuration. If the matrices are square, the solution is

$$\mathbf{Y} = \mathbf{VP}^{-1}$$

or

$$\mathbf{Z} = \mathbf{PV}^{-1}$$

respectively. For the special direct cases defined in (4.1), either \mathbf{P} or \mathbf{V} are diagonal matrices filled with the excitation pressures or velocities for each single patch. Their inversion leads to (2.19) and (2.20) respectively. If more measurement configurations than the number of patches are made, the system is overdetermined and may lead to better accuracy. It can be solved by using statistical methods.

2.6 Numerical results

For the numerical implementation and validation of the approach, Finite Element solvers were implemented in the open source software FreeFEM++ [Hecht et al., 2007]. The patch transfer matrices were obtained by successive blocking and iteration over the patches of the relevant surfaces as described in 4.1.

An FEM simulation for an acoustic domain (Equation (1.14)) was implemented. The surface and transfer impedance for a rectangular cavity ($0.7 \times 0.3 \times 1.0$ m) and for one with one half of the height ($0.7 \times 0.3 \times 0.5$ m) were determined with a patch

size of 0.1×0.1 m. To ensure that all modes in the frequency range up to 1 kHz are represented accurately, tetrahedral elements on a grid with a spacing of 0.05 m and quadratic Lagrangian shape functions (P2) were used.

2.6.1 Coupling two acoustic domains

The transfer functions from two small cavities coupled with the scheme described in 2.4.1 were compared to the the full cavity (Figure 2.5).

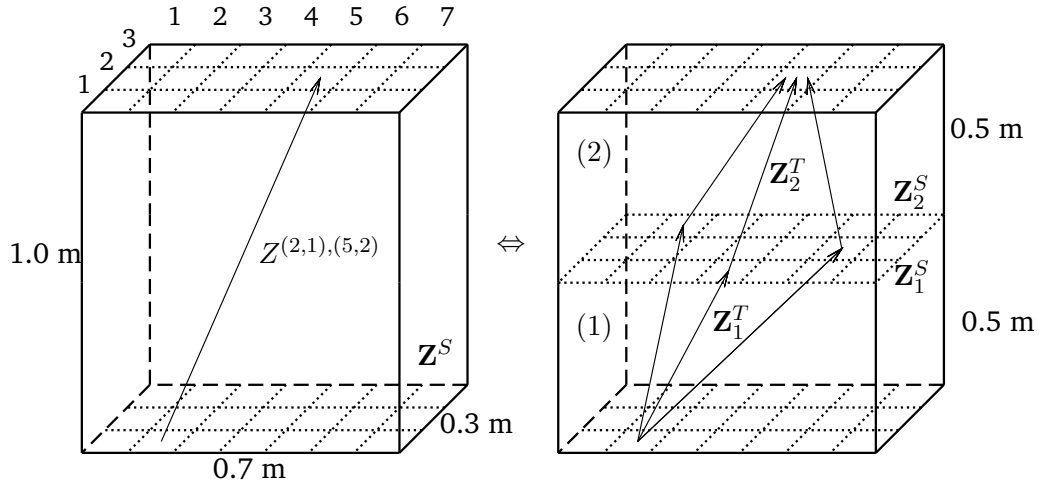


Figure 2.5: Test problem of a rigid cavity split in halves. The patch coordinates are labeled with (x, y) and the transfer functions are denoted by \mathbf{Z}

The results of the calculation are shown in Figure 2.6. The curves show near perfect match up to 1 kHz, which is in agreement with the half-wavelength criterion described by Ouisse et al. [2005].

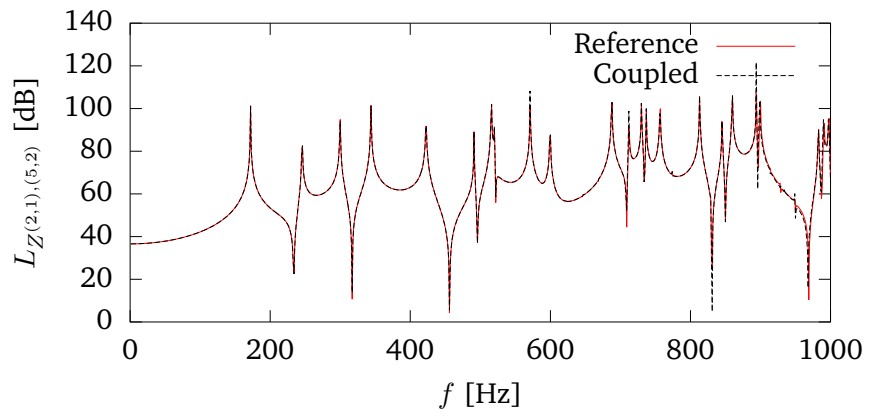


Figure 2.6: Comparison of the response of two patch-coupled rigid-walled rectangular air cavities. The graph shows a logarithmic plot of the transfer function, L_Z between the two patches (2, 1) and (5, 2) (see Figure 2.5)

Chapter 3

Test Case and Numerical Models

To evaluate the performance of the PTF coupling procedure and to develop experimental characterization methods, a simplified vibroacoustic system was chosen as a test rig. The system consists of a rigid air cavity, backed by a steel plate. Additionally, the plate is treated with an absorptive poroelastic foam layer. The components of the system are modeled using the Finite Element Method [Hecht et al., 2007] and analytic solutions.

3.1 Test rig parameters

Figure 3.1 shows the dimensions of the setup. The coupling surfaces are split into 8 patches of 40×40 cm. Since the front plate is clamped, it is assumed that the gaps of 50 mm at the left and right side do not contribute significantly to the response and can be neglected.

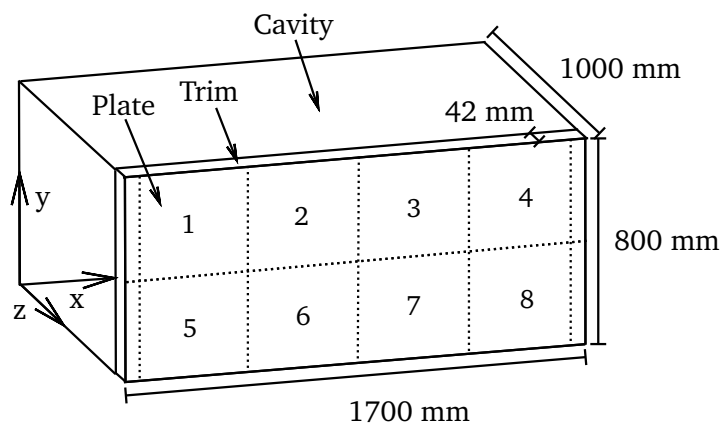


Figure 3.1: Vibroacoustic test rig with a steel plate (2 mm thickness, clamped rim), a damping layer and an air cavity.

To compare the system coupled by PTF with the physically assembled structure, three microphone positions are defined inside the cavity, as shown in Figure 3.2.

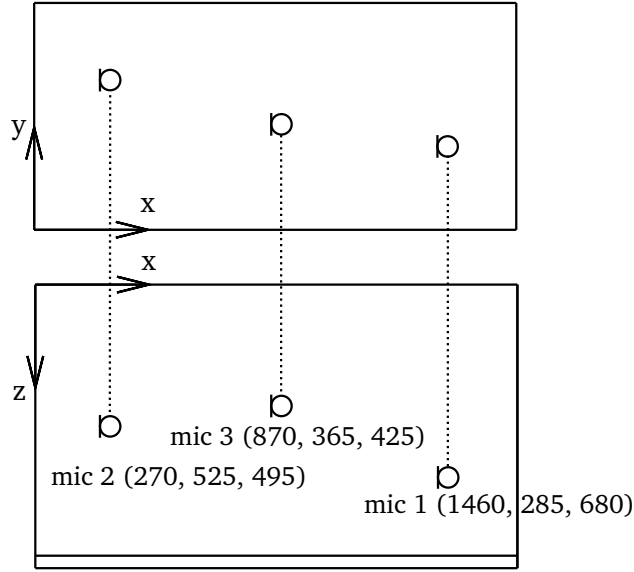


Figure 3.2: Microphone positions inside the cavity (dimensions in mm).

3.2 Air cavity

The air cavity of the test setup is backed by painted concrete walls to minimize absorption. Because of the rectangular symmetry and the quasi-rigid walls, it was assumed that it behaves like an ideal fluid cavity as defined in section 1.2. The numerical cavity characterization was therefore realized only in a numerical model which is described below. The model for the air cavity was realized in both, a modal superposition calculation (1.6.2) and an FEM model.

3.2.1 Numerical model: Modal superposition

For the rectangular rigid cavity of dimensions L_x , L_y and L_z , the eigenmodes of the Helmholtz equation (1.23) are cosine functions,

$$\phi_i(\mathbf{r}) = \frac{\zeta_i}{\sqrt{L_x L_y L_z}} \cos\left(\frac{m_{x,i} \pi x}{L_x}\right) \cos\left(\frac{m_{y,i} \pi y}{L_y}\right) \cos\left(\frac{m_{z,i} \pi z}{L_z}\right)$$

where $m_{x,i}$, $m_{y,i}$, $m_{z,i}$

$$\zeta_i = \sqrt{2^s}, \quad s = \text{sgn}(m_{x,i}) + \text{sgn}(m_{y,i}) + \text{sgn}(m_{z,i}).$$

The Eigenfrequencies are given by

$$\omega_i = \frac{\pi}{c} \sqrt{\left(\frac{m_{x,i}}{L_x}\right)^2 + \left(\frac{m_{y,i}}{L_y}\right)^2 + \left(\frac{m_{z,i}}{L_z}\right)^2}.$$

The resulting patch transfer functions can be obtained by integrating the modal contributions across a patch according to (2.3). The analytic expression for a patch-to-point



Figure 3.3: Interior of the air cavity for the PTF validation measurements. Microphones 1, 2 and 3 are visible.

transfer function on the xy surface of a rectangular cavity is given by Pavic [2010] as

$$Z^T(\mathbf{r}, \mathbf{r}') = i\omega\rho c^2 \frac{\phi_i(\mathbf{r})\phi_i(\mathbf{r}')}{\omega_i^2 - \omega^2 + 2i\varepsilon\omega} \operatorname{sinc}\left(\frac{m_{x,i}\pi\Delta x'}{L_x}\right) \operatorname{sinc}\left(\frac{m_{y,i}\pi\Delta y'}{L_y}\right).$$

$\mathbf{r} = (x, y, z)$ denotes the point position inside the domain and $\mathbf{r}' = (x', y', 0)$ are the coordinates of the center of the patch. $\Delta x'$ and $\Delta y'$ are the dimensions of the patch. The patch-to-patch impedance between two patches of size Δx , Δy and $\Delta x'$, $\Delta y'$ centered at \mathbf{r} and \mathbf{r}' respectively, is given by

$$Z^S(\mathbf{r}, \mathbf{r}') = i\omega\rho c^2 \frac{\phi_i(\mathbf{r})\phi_i(\mathbf{r}')}{\omega_i^2 - \omega^2 + 2i\varepsilon\omega} \operatorname{sinc}\left(\frac{m_{x,i}\pi\Delta x}{L_x}\right) \operatorname{sinc}\left(\frac{m_{y,i}\pi\Delta y}{L_y}\right) \operatorname{sinc}\left(\frac{m_{x,i}\pi\Delta x'}{L_x}\right) \operatorname{sinc}\left(\frac{m_{y,i}\pi\Delta y'}{L_y}\right).$$

The equivalent damping ε due to a small wall absorption coefficient $\alpha \ll 1$ ($\approx 0.5\%$ for the given cavity) is given by

$$\varepsilon = \alpha c \left(\frac{1}{L_x} + \frac{1}{L_y} + \frac{1}{2L_z} \right). \quad (3.1)$$

This formula is based on the following simplification: The amplitude of a wave propagating with c is assumed to be reduced by α when traveling across the cavity length. In the z -direction the damping is only half of the values in the other directions, since one xy surface is used for the coupling. This surface is blocked per definition and therefore rigid without any damping.

3.2.2 Numerical model: Finite element method

For more complex geometries, the analytical treatment of the acoustic equation is not possible anymore. Also, the equivalent damping assumption (3.1) fails if the wall absorption is high. For this reason, another model based on the finite element method (A.1.2) was developed. In such a model, it is possible to apply an impedance boundary condition

$$p^S(\mathbf{x}) = Z^S v^S(\mathbf{x})$$

on the walls. The well-known surface impedance for a reflection factor $r = 1 - \alpha$ is given by

$$Z^S = \rho_0 c_0 \frac{1 + r}{1 - r}.$$

For the model, tetrahedral elements of second order with a grid spacing of 5 cm have been used. A comparison between the analytic modal solution and the FEM model results is shown in Figure 3.4. The FEM model accuracy deteriorates with higher frequencies but is still in the acceptable range. The equivalent damping assumption for the modal solution matches the wall absorption model of the FEM.

3.3 Backing plate

3.3.1 Numerical model

For the steel plate, a model of the Kirchhoff-Love thin plate formulation (see (1.4)) was implemented. Its density was estimated to $\rho = 7850 \text{ kg/m}^3$ and the E -modulus of standard steel, $E = 2.05 \cdot 10^{11} \text{ N/m}^2$ was assumed in the simulation. For the fourth order plate equation, standard finite element interpolations perform poorly or fail. One of the simplest elements that yield satisfactory results for this type of equation are non-conforming elements of second order as described by Morley [1968]. A fine element size of 1 cm compared to the wavelength of $\lambda \approx 13 \text{ cm}$ at $f = 1000 \text{ Hz}$ was chosen, since Morley elements tend to underestimate the eigenfrequencies of the plate equation [Rannacher, 1979].

3.4 Porous layer

To introduce damping to the system, a layer of an open-cell foam (“Basotect TG”) was inserted between the plate and the cavity. The open-cell foam was modeled with the Delany-Bazley method (section 1.5) using the flow-resistivity of $11350 \text{ N m}^{-4} \text{ s}$ measured by the manufacturer. The Young modulus is given by $E = 144393 \text{ N/m}^2$. An FEM calculation was performed to obtain a numerical characterization of the terms of the impedance matrix.

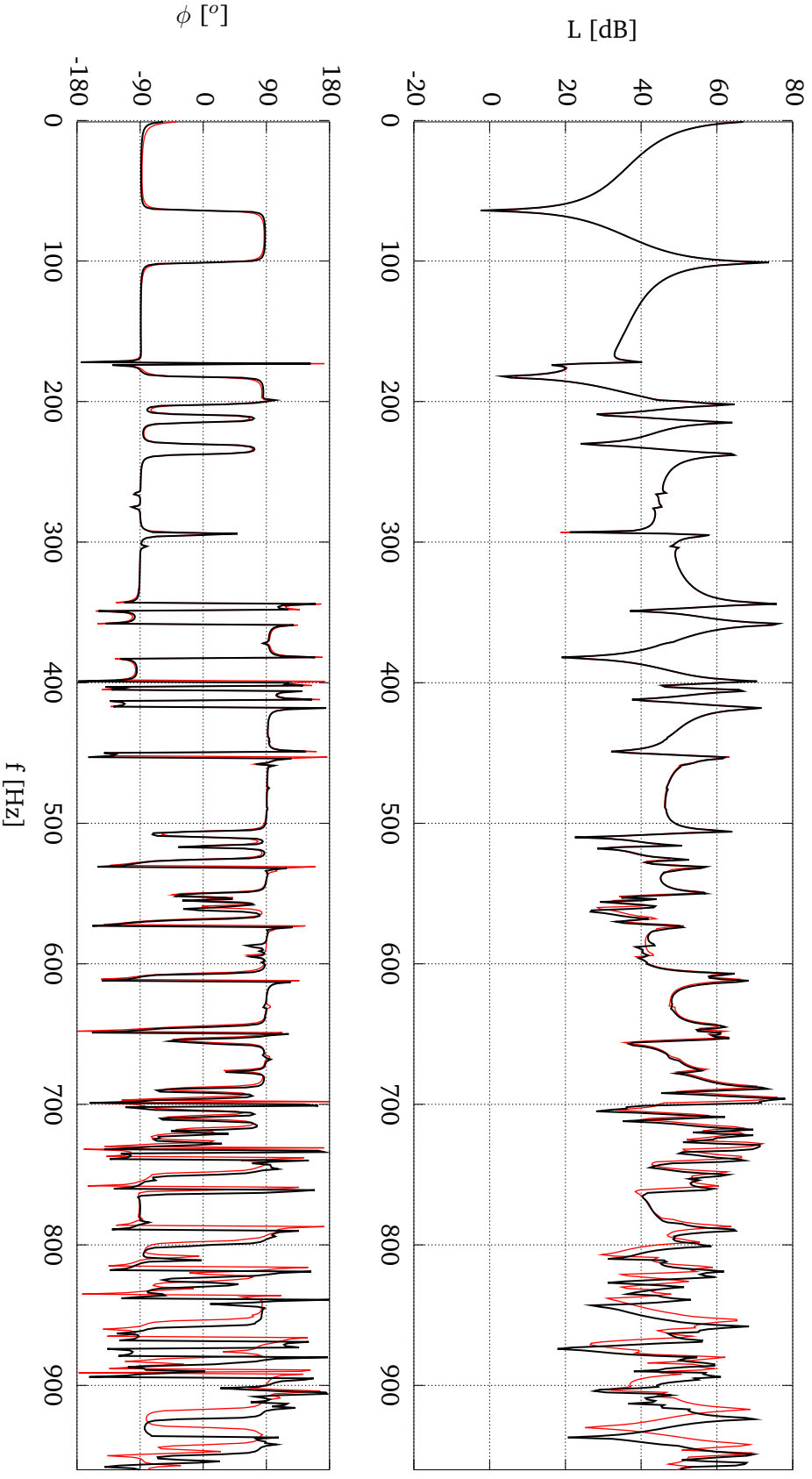


Figure 3.4: Comparison between the analytic modal superposition (3.2.1, red) and the FEM solution (3.2.2 black) for the transfer function from patch 5 to microphone 2.



Figure 3.5: Front view of the test rig with the attached steel plate. For measurements of the component PTF of the plate, the opposite surface of the cavity can be removed

Chapter 4

Experimental Subsystem Characterization

A characterization method for a system only has to measure the transfer functions over the relevant boundaries and the excitation positions. If the remaining boundary conditions are not changed, this will yield the matrix that corresponds to the condensed \mathbf{Y} or \mathbf{Z} matrix as specified in (2.3.1). In the experimental characterization it has to be ensured that the only transfer path from the excitation position to the system interior is through the characterized surface. Only in this case, the assumption of condensed transfer functions (2.3.1) holds.

In this section, several component characterization methods based on the principal developments in section 2.5 are proposed. Experimental data for the characterization and validation measurements were provided by Giorgio Veronesi of the Virtual Vehicle Competence Center [Nijman et al., 2012].

4.1 Structural surface mobility

The direct method to obtain the surface mobility of a structure has been briefly described for numerical calculations (2.5.1). To obtain the mobility of a structural surface, the surface pressures have to be close to zero except for the excitation. A patchwise pressure excitation is not easy to realize on a structure from the experimental point of view. However, a superposition of point forces should converge to a uniform pressure excitation for a large number N_i of excitation positions on the source patch i . On the receiving patch j , the average velocity is measured by N_j sensors. The real mobility term is then given by

$$Y_{ij} = \frac{v_j}{p_i} \approx \frac{1}{N_i N_j} \sum_{k=1}^{N_j} \sum_{l=1}^{N_j} \frac{v_{jkl}}{p_{ikl}} = \frac{1}{N_i N_j} \sum_{k=1}^{N_j} \sum_{l=1}^{N_j} Y_{ijkl}. \quad (4.1)$$

The patch mobility Y_{ij} is therefore given by the linear average of the transfer functions Y_{ijkl} for each excitation point k on patch i and receiving point l on patch j .

In the experimental realization, one patch is excited with an impulse hammer at sev-

eral positions and the response is measured on the receiving patch. If the average transfer function Y_{ij} does not change anymore when adding new hammer blows, we can assume that convergence has been reached. A numerical test for this behavior is shown in Figure 4.1. The approximated patch mobilities by excitation on a regular grid with equidistant points in x and y direction and random excitation configurations are compared to a patch-wise uniform pressure excitation. The excitation is performed on patch 1 and the average velocity is measured on patch 3.

From the numerical results we can draw the conclusion that for the specified test case, a regular grid of 16 (4×4) excitation positions is sufficient for a good approximation of the patch mobility up to a frequency of $f \approx 800$ Hz. Random positioning of the points leads to a larger error, even for more excitation positions. This result could be caused by the non-optimal area coverage by independent random positions. For the regular grid, there are no large gaps between the grid nodes. Due to reciprocity (1.26) the same assumption holds for sensor positions on the receiving patch.

There are two possibilities to measure the receiving patch velocity:

Firstly, we can measure the structural velocity directly by attaching accelerometers to the surface. The other option is to measure the velocity of the air close to the surface. This can be realized by using an array of particle velocity sensors as described by de Bree et al. [1996].

For the measurements of the plate defined in (3.1) a grid of 16 accelerometers was installed on each receiving patch. A comparison between the simulated plate mobility and the experimental data can be found in Figure 4.2. The overestimation of the transfer mobilities at 400 Hz and above 800 Hz corresponds to the numerical test in Figure 4.1. At 400 Hz, the wavelength in the plate is approximately 20 cm, which is half of the patch width (see also 5.2). Therefore a uniform pressure leads to a strong cancellation of waves propagating from the excitation position. At high frequencies and lower wavelengths, more and more plate modes are cancelled inside the uniform patch but not by the point grid.

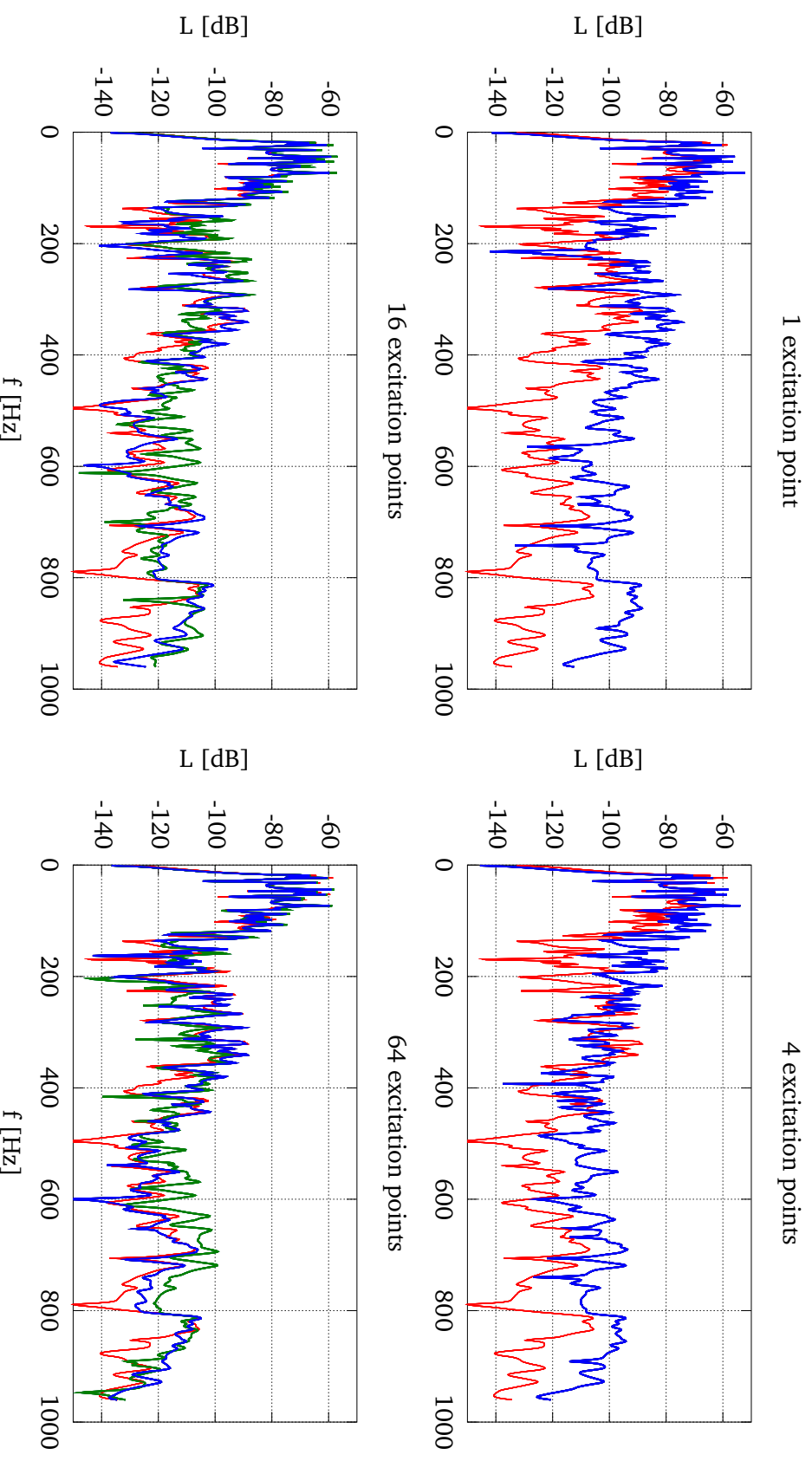


Figure 4.1: Simulated approximate patch mobility (4.1) $Y_{1,3}$ depending on the number of excitation positions. Excitation in a regular grid (blue) yields better agreement with the uniform excitation (red) than random excitation (green). (40 cm PTF)

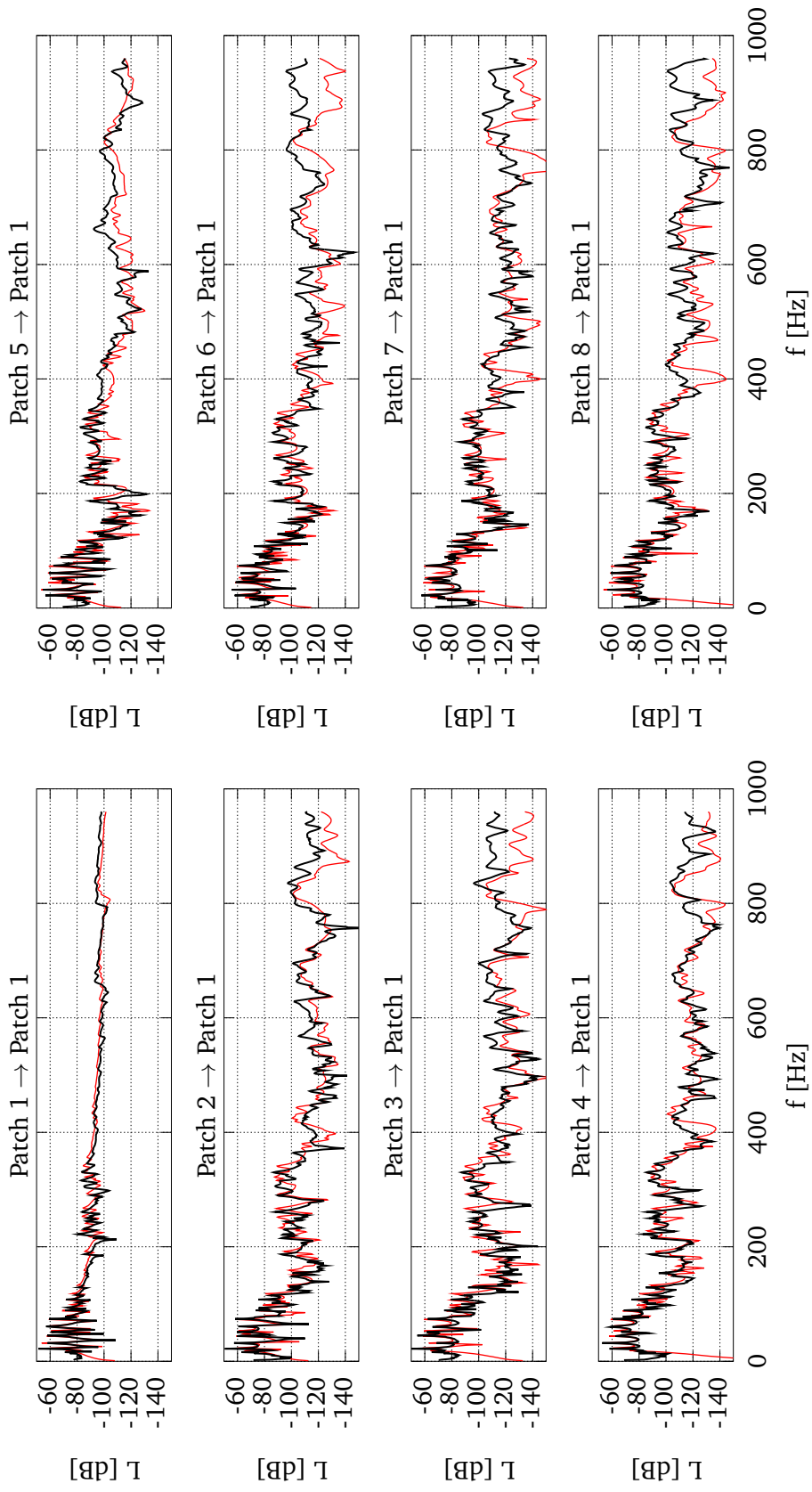


Figure 4-2: Comparison between the simulated (red) and measured (black) patch mobilities Y_{i1} of the test rig's steel plate. (40 cm PTF)

4.1.1 Influence of the environment

We use the direct method to measure the mobility \mathbf{Y} of an elastic structure embedded into a fluid with surface impedance \mathbf{Z}_0 . From the coupled equation of structure and surrounding fluid (2.14), we obtain

$$(\mathbb{I} - \mathbf{Y}\mathbf{Z}_0) \mathbf{v}^S = \mathbf{Y} \mathbf{p}^F .$$

The experimentally measured mobility $\hat{\mathbf{Y}}$ is influenced by the reaction forces from the coupled fluid. It describes the ratio between the surface velocity \mathbf{v}^S of the immersed structure and the force excitation \mathbf{p}^F ,

$$\mathbf{v}^S = \hat{\mathbf{Y}} \mathbf{p}^F .$$

Therefore, it fulfills the equation

$$\hat{\mathbf{Y}} = (\mathbb{I} - \mathbf{Y}\mathbf{Z}_0)^{-1} \mathbf{Y} . \quad (4.2)$$

For small values of $\mathbf{Y}\mathbf{Z}_0$ with respect to unity, the measured mobility $\hat{\mathbf{Y}}$ matches the real mobility \mathbf{Y} . Otherwise the measurement has to be corrected with the impedance of the environment. The exact result is

$$\mathbf{Y} = \left(\hat{\mathbf{Y}}^{-1} + \mathbf{Z}_0 \right)^{-1} .$$

Morse and Ingard [1986] provide an approximation for the radiation impedance of a rectangular piston of dimensions $a \times b$ in an open air space,

$$Z_r = \frac{k^2(a^2 + b^2)}{16} - \frac{8i(a^2 + ab + b^2)}{9\pi(a + b)} .$$

For the 2mm steel plate defined in the test case no significant effect was observed by loading the plate with the additional radiation impedance. However, when the plate is coupled to the cavity, there are some changes at specific resonance frequencies of the cavity. The results of a numerical test case can be found in Figure 4.3.

If the transfer mobility of the plate is low, the transfer path via the reflections inside the air cavity dominates and leads to a higher effective mobility. This behavior is limited to few cavity resonances around 10 Hz, 170 Hz, 500 Hz and 900 Hz. Additional damping material in the cavity could reduce these effects. All in all, the fluid loading plays a minor role for the characterization of structures with mobilities similar to the test plate.

4.2 Fluids and porous materials

In principle, the surface impedance of a fluid (this includes porous materials seen as fluids) can be characterized in a direct way: The surface velocity \mathbf{v}^S has to be set to zero by blocking the boundary with a rigid surface. In the characterization proce-

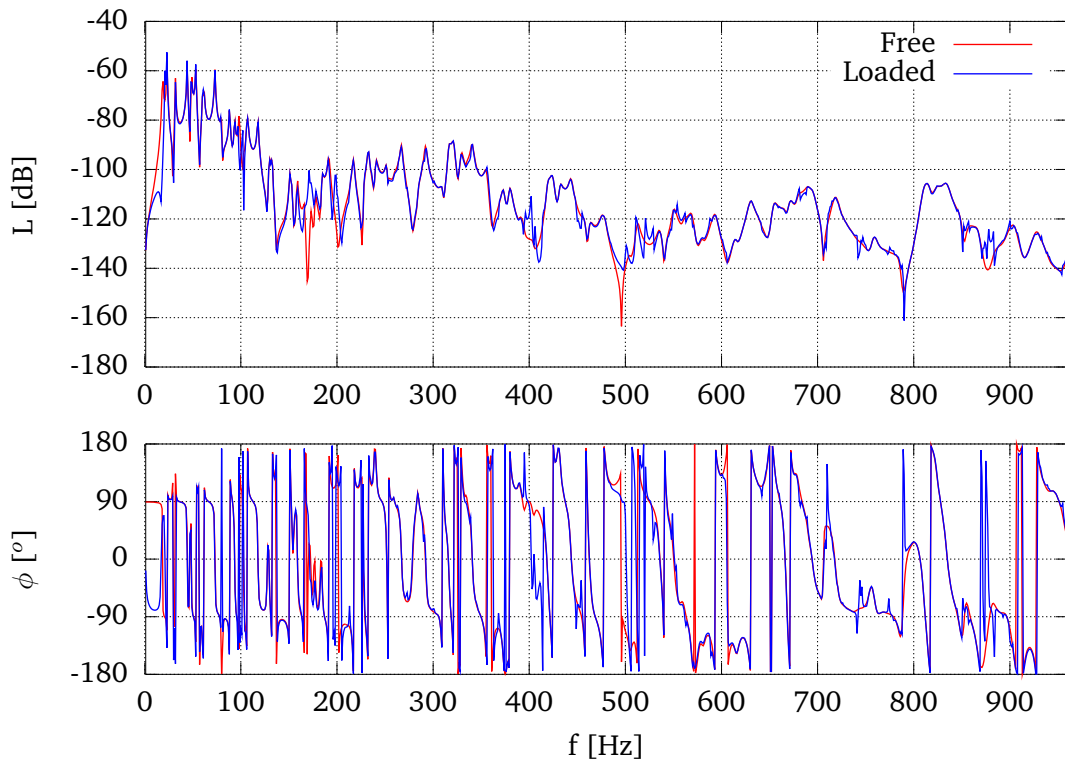


Figure 4.3: Comparison of the term Y_{13} of the effective mobility of the plate coupled to the air cavity (blue) with the one from the free plate (red).

ture, this surface should be moved patch-wise and the corresponding pressures are measured on the receiving patches.

There are several criteria for the blocking surface. It should have a sufficiently high impedance while being able to be moved patch-wise and have its first modes above the characterized frequency range. Otherwise the assumption of a uniform excitation does not hold. It is, however, questionable, if a uniform excitation is really needed. If the dimension of the patches is much smaller than half a wavelength, only the mean value of the excitation should play a role. Only when the frequency limit of the method is reached (see 5.2), a well-defined spatial distribution of the excitation becomes important.

4.2.1 Indirect method

In experiments, it is often not possible to set v^S to zero by blocking the surface. If this is the case, the indirect method described in (2.5.2) can be applied. A layer of porous material is placed in an air environment. If the cross-terms of impedance matrix between the front and the back surface should be characterized, the sample can be mounted hanging. If just the surface terms are needed, it is sufficient to place it on a rigid floor.

Since both surface pressure and surface velocity have to be obtained, an array of PU probes [de Bree et al., 1996] is the ideal sensor for this method of measurement.

4.2.2 Simplifications

For highly damped porous materials the waves decay very fast when propagating inside. As a result, the terms of the impedance matrix for patches far away from each other are small. If the material is assumed to be locally reacting, only the input terms Z_{ii} , describing the response on the excitation patch itself, are considered. Adding next-neighbor terms (for example Z_{12}) or terms for patches that are further away (e.g. Z_{13}), not only the accuracy of the description but also the number of required measurements will increase. In this case, the result will be a banded matrix describing the most important terms for the non-local behavior of the material.

For the trim described in (3.1), an FEM calculation shows that the decay of the excitation is very fast (Fig. 4.4). Even the transfer impedance between the diagonally adjacent patches can be neglected (see Fig. 3.1 for the patch configuration). The impedance depends mainly on the relative position between the patches ($Z_{11} \approx Z_{22}$, $Z_{12} \approx Z_{23}$, ...). Therefore it is possible to simplify the problem to two patches in the middle of the foam and use the results for all patches. The input and transfer impedance between the two patches has to be measured while the remaining surface is blocked.

The second simplification is valid for thin material layers: If the thickness of the layer is small compared to the wavelength and the decay distance in the material, the blocked pressures on both sides is nearly equal. As a result, the matrix elements connecting the two sides, $Z_{ij}^{S_1 S_0}$ (see Fig. 2.4) will be the the same as the ones on one surface, $Z_{ij}^{S_0}$. In this case, the material is quasi-two-dimensional and it is sufficient to construct the matrix for one side.

The trim described in (3.1) is 42 mm thick. Numerical results show, that in here the impedance terms connecting the two sides are a good approximation to the terms on one side (Fig. 4.5) up to $f = 500$ Hz. The results deteriorate at high frequencies.

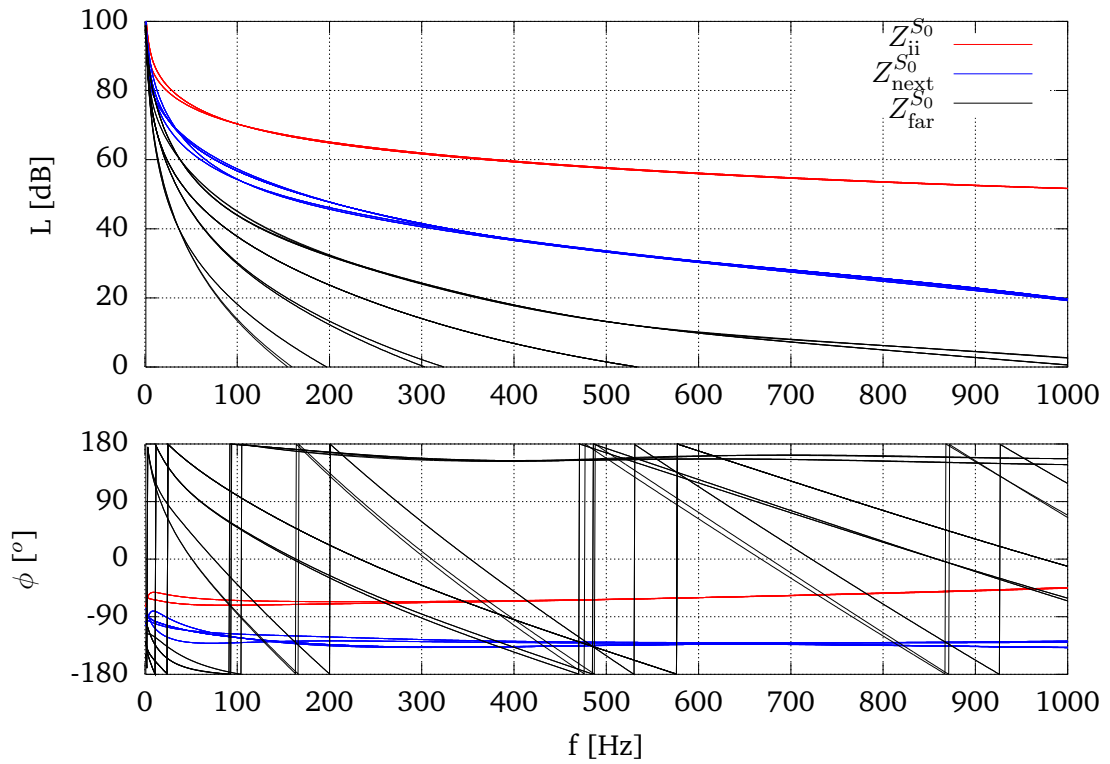


Figure 4.4: Impedance matrix terms. The transfer terms to far patches (black) are negligible in comparison to the input (red) and next neighbour (blue) terms.

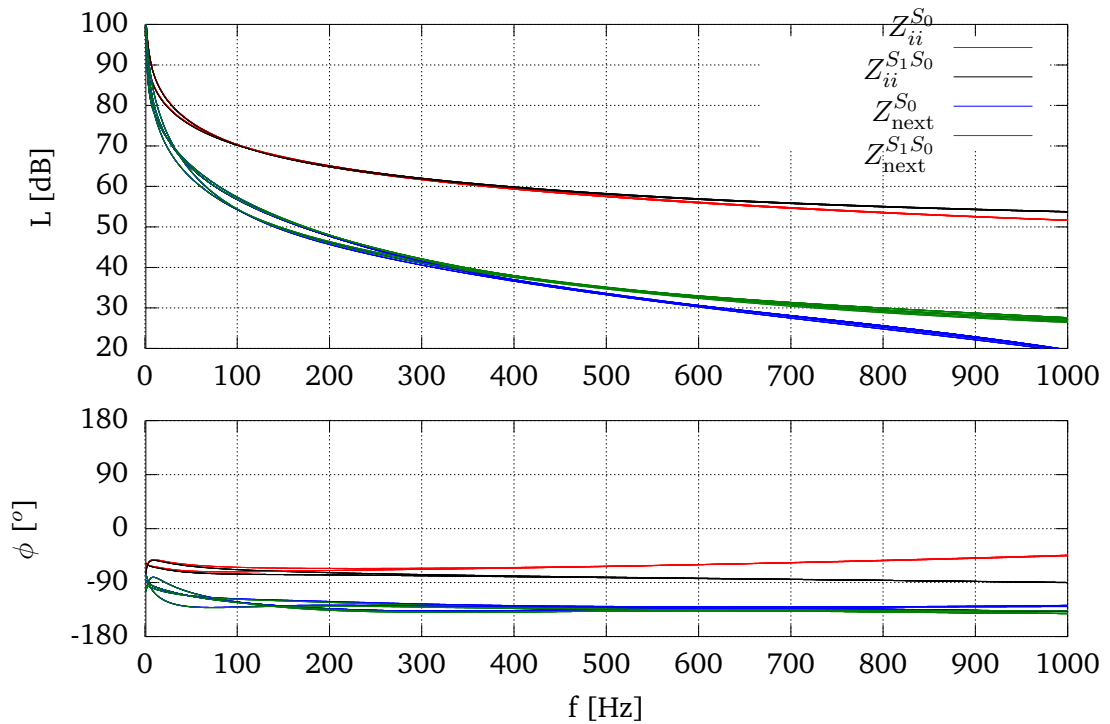


Figure 4.5: Trim sample transfer impedances $Z_{ij}^{S_1S_0}$ across the thickness (black, green) compared to the terms on surface 0, $Z_{ij}^{S_0}$ (red, blue).

4.2.3 Measurements and results

For the considered trim material, both direct (Figure 4.6) and indirect (Figure 4.7) characterization were performed. The direct method was applied to a piece of 40×80 cm and the indirect method on two neighboring patches in the center of the full foam sample. The blocking of the patches for the direct method was realized with steel plates of dimensions $200 \times 200 \times 22$ mm. Their high mass and their first eigenfrequencies above 2 kHz provide a good blocking condition. Both methods yield similar results to the numerical model (3.4), which is shown in Figure 4.8 - 4.11. The agreement below $f = 100$ Hz is poor, which can be explained by the following reasons:

- For the direct method, the plates were lying on top of the foam, so a mass-spring resonance at 22 Hz limits the validity of the low-frequency results.
- For the indirect method, noise starts to appear at $f < 100$ Hz and the Delany-Bazley model is not valid at low frequencies due to the non-rigidity of the structure [Delany and Bazley, 1970].

The higher transfer impedance of the direct method is likely the result of the smaller sample size in comparison to the model for the simulated transfer functions. Further investigations are needed to clarify this topic in detail.

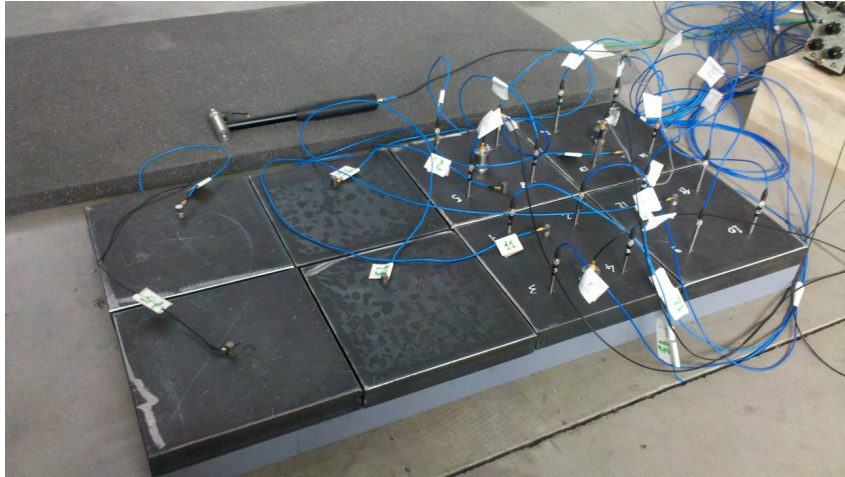


Figure 4.6: Direct foam characterization method. The steel patches are excited with an impact hammer and the pressure underneath is measured by microphones

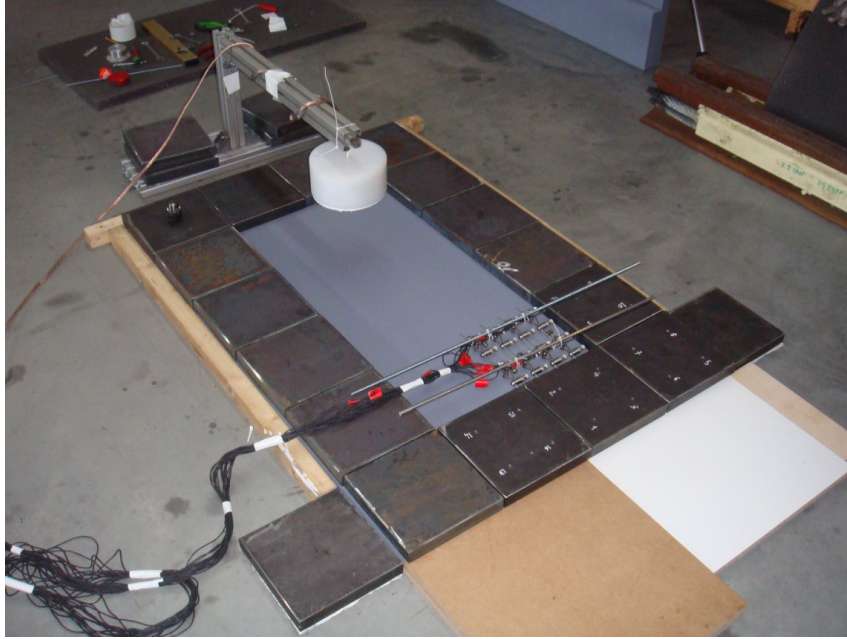


Figure 4.7: Indirect foam characterization method. The patches are excited by a loudspeaker and the surface pressures and velocities are measured with a PU probe

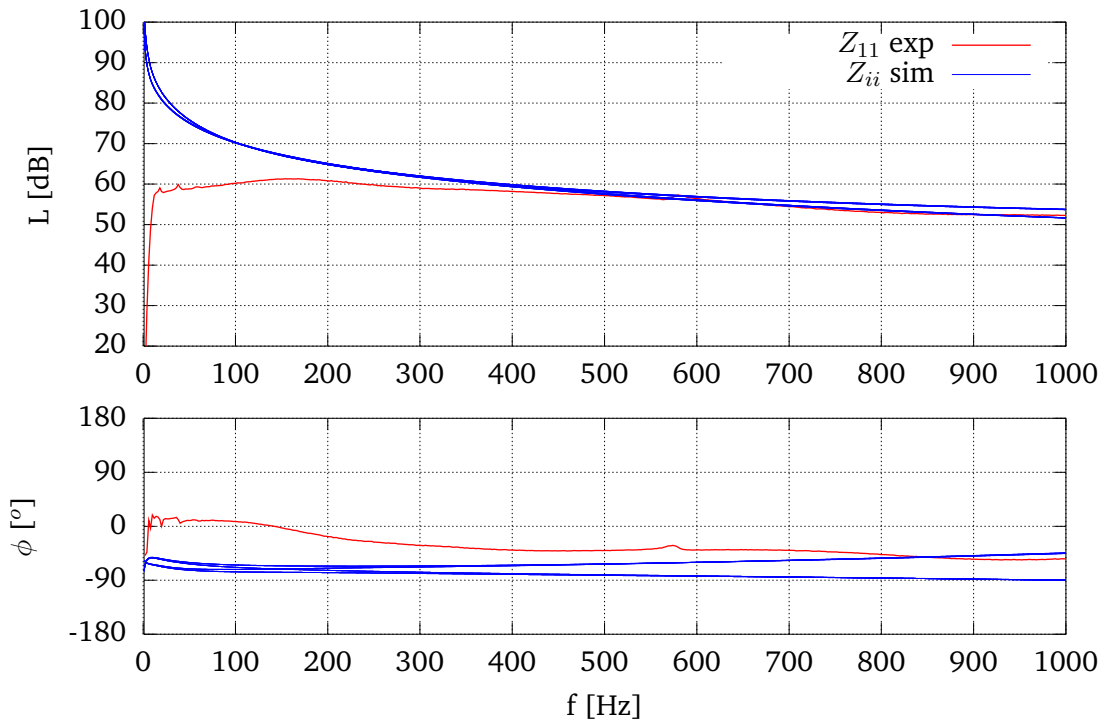


Figure 4.8: Patch input impedance obtained by the direct method (4.2) compared to simulated input impedances

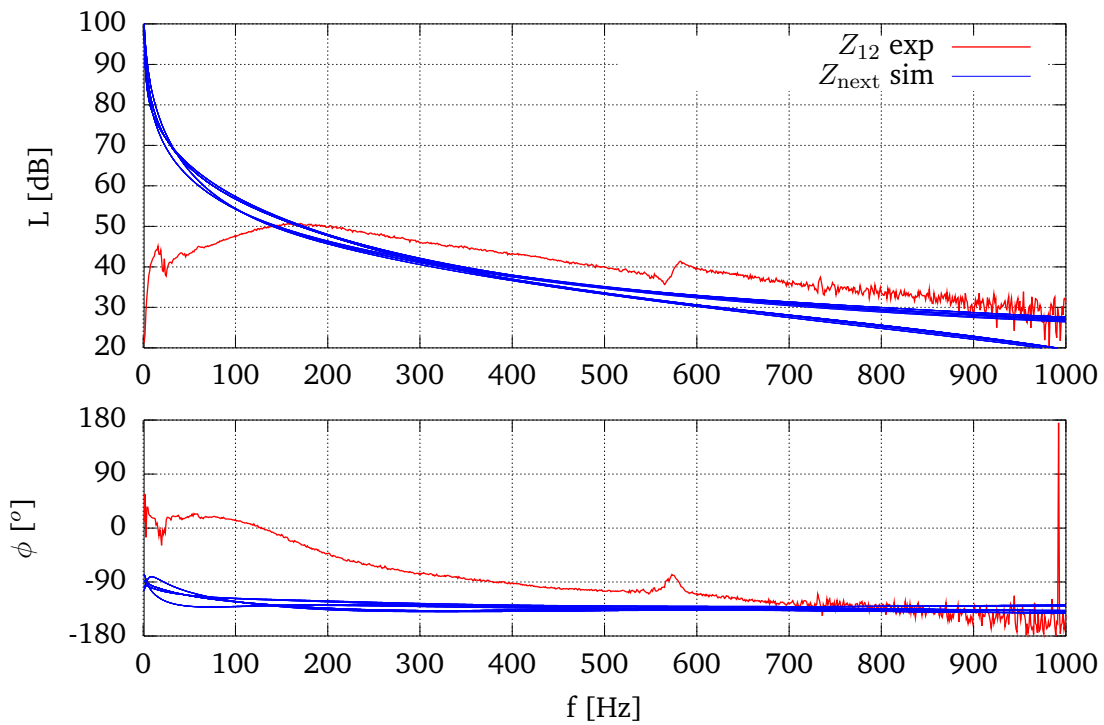


Figure 4.9: Patch transfer impedance obtained by the direct method (4.2) compared to simulated input impedances

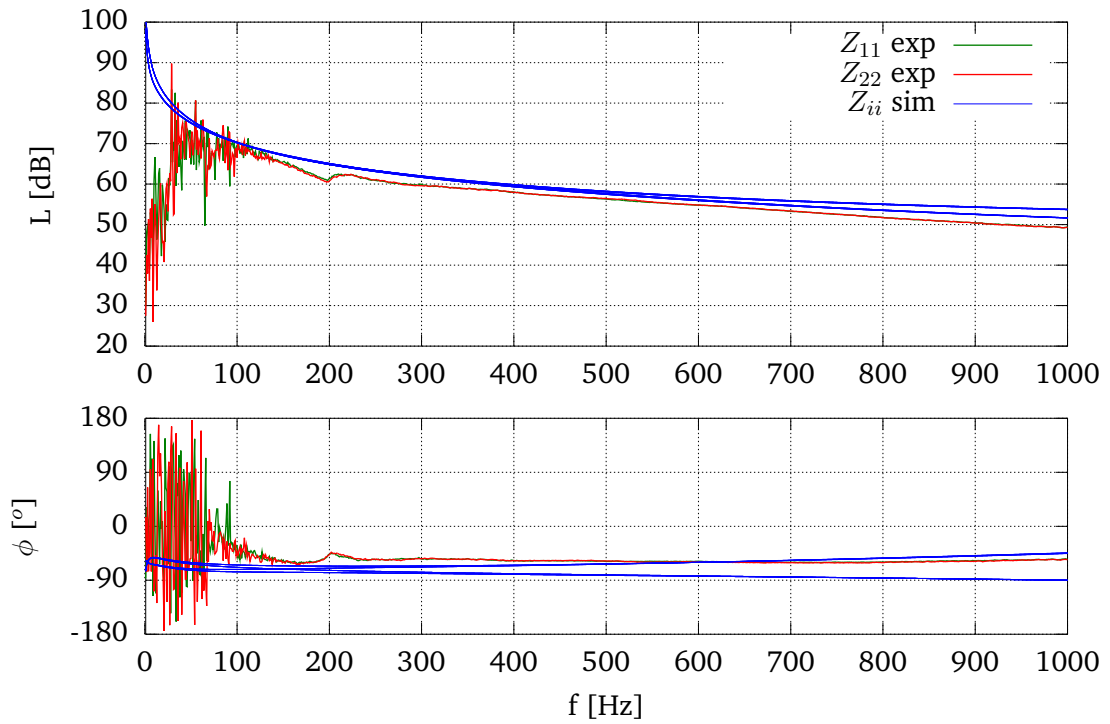


Figure 4.10: Patch input impedance obtained by the indirect method (4.2.1) compared to simulated input impedances

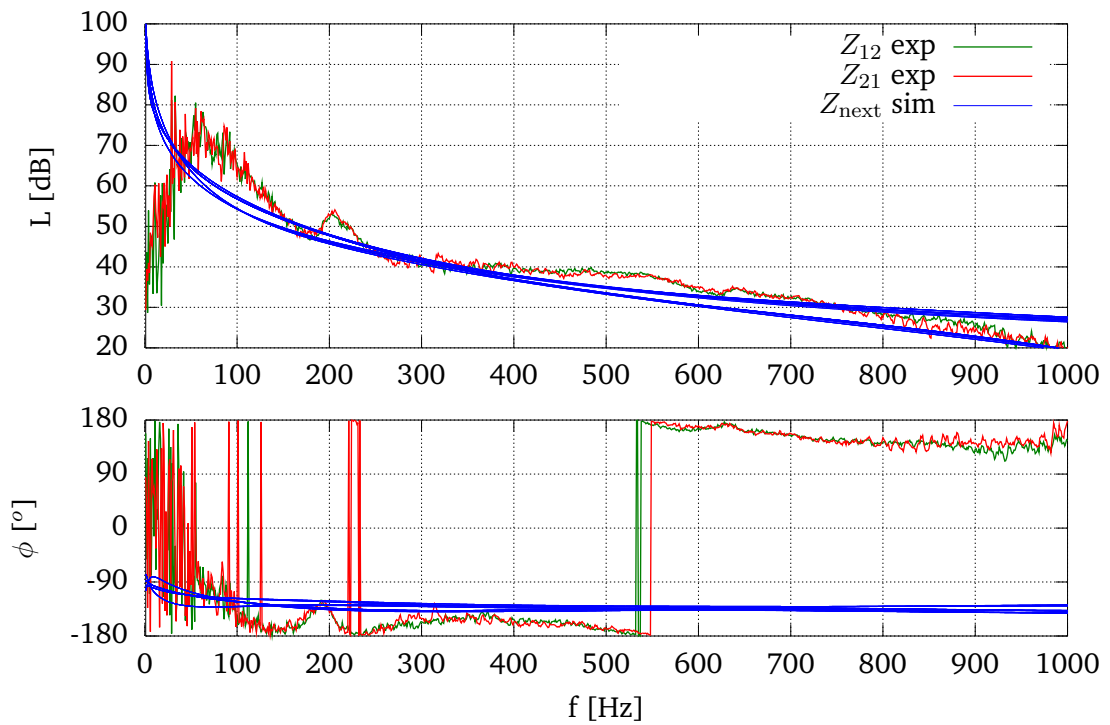


Figure 4.11: Patch transfer impedance obtained by the indirect method (4.2.1) compared to simulated input impedances

Chapter 5

Limitations of the Method

The approximation of space-dependent physical or numerical functions by uniform patch averages reaches its limit when the fluctuation pattern within a patch cannot be captured by the coarse resolution of the patch grid. In this case, assumption 2.10 that the discretized surface mobility is approximately equal to the inverse of the discretized surface impedance, does not hold anymore. If this is the case, the approximation is not consistent anymore and should fail. In this chapter, we are going to analyze these effects to gain a better understanding of the limitations of the method.

5.1 Conceptual analysis of averaging errors

To illustrate the method limitations for heterogenous media, let us take a general example (Figure 5.1) of a patch average over two parallel systems with impedances

$$Z_1 = F_1/v_1 = Y_1^{-1} \text{ and} \\ Z_2 = F_2/v_2 = Y_2^{-1} .$$

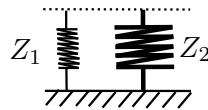


Figure 5.1: System of two springs with impedance average taken on the top surface.

The idea is, that for a velocity excitation, the reaction force (or pressure) will be given mainly by the system with the higher impedance. On the other hand, if we excite with a force, the system with the high mobility will move more and increase the average velocity. Let us take a look at the two cases of direct impedance and direct mobility measurements.

Case 1: Direct impedance measurement (velocity excitation)

The system is excited with a common velocity,

$$v = v_1 = v_2 ,$$

and responds with the sum of the two force responses,

$$\begin{aligned} F &= F_1 + F_2 \\ &= Z_1 v + Z_2 v . \end{aligned}$$

The measured combined impedance is therefore given by the sum of the two impedances,

$$Z = F/v = Z_1 + Z_2 . \quad (5.1)$$

Case 2: Direct mobility measurement (force excitation)

The system is excited with a common pressure. If we assume, that each spring covers half the patch, each spring feels half of the force,

$$F_1 = F_2 = \frac{1}{2} F .$$

The response is an average velocity,

$$\begin{aligned} v &= \langle v_1, v_2 \rangle = \frac{1}{2} (v_1 + v_2) \\ &= \frac{1}{2} (Y_1 F_1 + Y_2 F_2) \\ &= \frac{1}{4} (Y_1 + Y_2) F \end{aligned}$$

The measured combined mobility is therefore given by the average mobility,

$$Y = v/F = \frac{1}{4} (Y_1 + Y_2) . \quad (5.2)$$

Comparison of the cases

The inverse of (5.2) yields

$$Y^{-1} = \frac{4}{Y_1 + Y_2} = \frac{4}{Z_1^{-1} + Z_2^{-1}} . \quad (5.3)$$

We note, that this is two times the harmonic mean of the impedances opposed to twice the arithmetic mean Z as defined in (5.1). They are only equal if $Z_1 = Z_2$.

Otherwise, the ratio of the two is given by

$$\begin{aligned}
 R = \frac{Z}{Y^{-1}} &= \frac{1}{4} (Z_1 + Z_2) (Z_1^{-1} + Z_2^{-1}) \\
 &= \frac{1}{2} + \frac{1}{4} (Z_1/Z_2 + Z_2/Z_1) \\
 &= \frac{1}{2} + \frac{1}{4} (X + X^{-1}) ,
 \end{aligned}$$

Where $X = Z_2/Z_1$. This ratio becomes one for $Z_1 = Z_2$ and therefore $Z = Y^{-1} = 2Z_1$. The discrepancy between positive and negative real factors X is shown in Figure 5.2.

For poro-elastic damping layers, this conceptual feature can be important: If a material consists of a skeleton and a fluid with different impedances and low coupling, it may be modeled as a parallel system of different impedances. In this case, it makes a difference, if it is coupled to a structure or to a fluid domain. The characterization procedure has to take this into account by exciting in a similar way as in the coupled system:

The indirect method (2.5.2) should yield better results on the surface that is later coupled to the fluid. In this case, the air in the pores is excited more efficiently than the skeleton. For the surface that is coupled to the structure, a forced velocity excitation using the direct method (2.5.1) is closer to the final boundary conditions. However, to find a definite answer to the problem of the right characterization method for heterogenous media, further investigations are required.

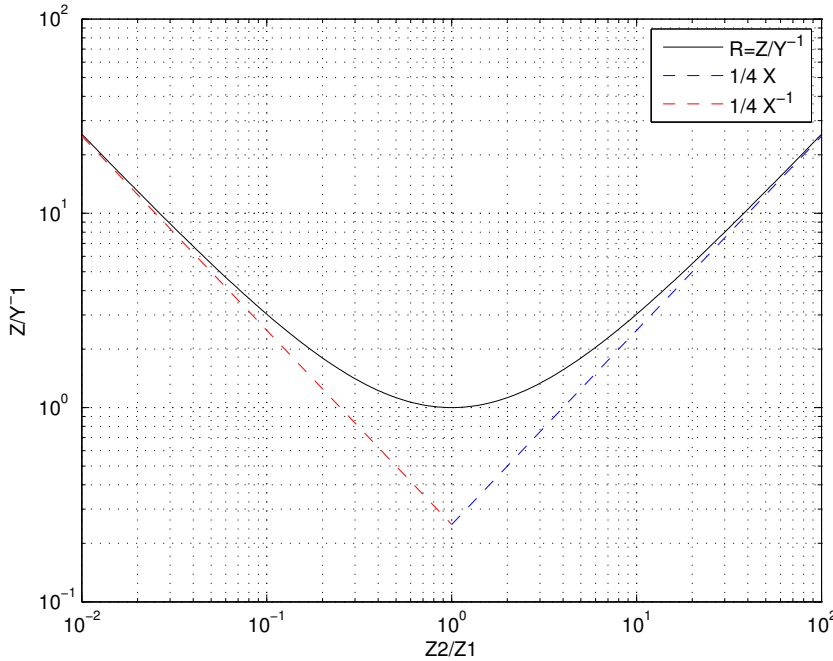


Figure 5.2: Patch impedance ratio $R = Z/Y^{-1}$ between v and F excitation.

5.2 Limitations due to the patch size

When the wavelength becomes smaller than two patches, the grid resolution is not sufficient anymore to capture the wave shape and aliasing will occur. As a comparison, the general rule for FEM with linear shape functions is the $\lambda/6$ criterion for the element size [Zienkiewicz and Taylor, 2000]. There is, however, a notable difference: PTF is based either on measurements or on a reasonably fine FEM model. From this accurate solution, the surface is then discretized with a coarse grid of patches. Therefore, the positions of the eigenfrequencies of each subsystem will not shift as it would be the case in the FEM due to element stiffening.

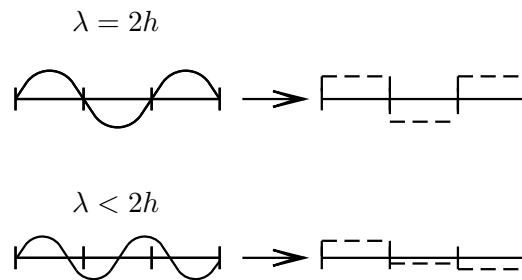


Figure 5.3: Patch size limit at the spatial Nyquist frequency.

The main limitation of PTF is that modes with a transverse wavelength below the diameter of two patches are missed (Figure 5.3). In this case, the patch grid is not able to represent the wave shape according to the Nyquist theorem and aliasing effects occur. This behavior has been verified by Ouisse et al. [2005] and a numerical test case is shown in Figure 5.4. The results suggest a $\lambda/2$ rule as a patch size criterion. The missed modes in the higher frequency range lead to an underestimation of the system response.

In the case of a structure with a short wavelength radiating into a fluid with longer wavelength, the frequency limit is given by the long fluid wavelength. This is explained in the following section 6.1.

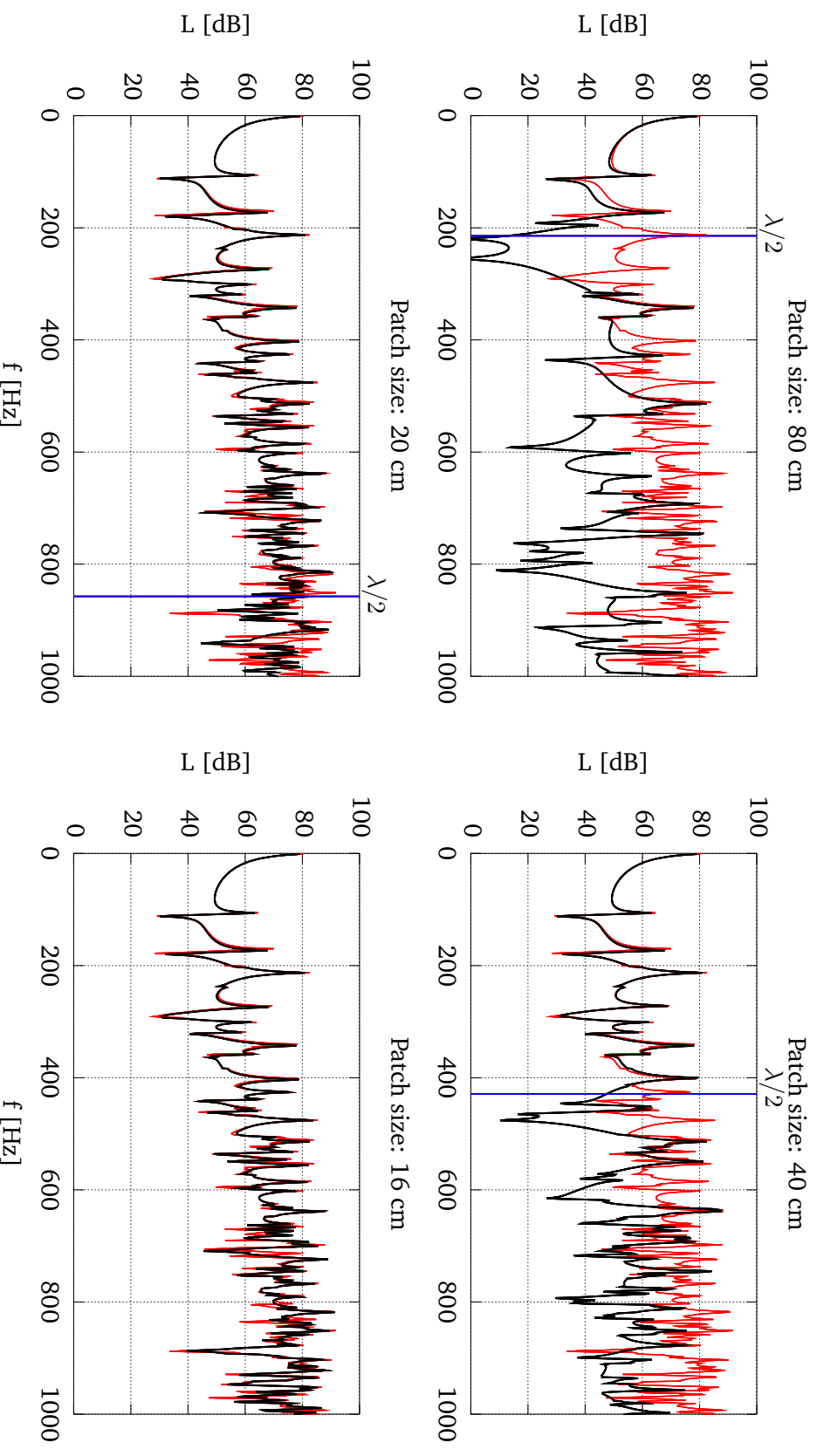


Figure 5.4: Transfer function between the points (1.36, 0.29, 0.32) and (0.76, 0.37, 0.58) inside a rigid cavity of $1.6 \times 0.8 \times 1.0$ m intersected by a PTF plane at $z = 0.4$ (dimensions in m). Comparison of PTF (black) to full cavity (red) solution.

Chapter 6

Results for the Assembled System

6.1 Bare plate + cavity

To evaluate the performance of the coupling method, the test rig was assembled without the porous layer (untrimmed). The resulting plate-cavity system was coupled with the PTF method according to (2.4.2). For the purely numerical model, also a finer grid of 20×20 cm was used on the coupling surface. The coupled system with 40×40 cm patches was realized both for the simulated and experimental plate characterization.

The plate was excited by 16 phased point forces on patch 5 of 40×40 cm and the response pressure inside the cavity was measured with microphones. Figures 6.1-6.3 show the results of this investigation.

A higher accuracy of the results should be expected when using a finer patch grid. For a patch dimension of 40 cm, the $\lambda/2$ limit for the wavelength in air is located at $f = 430$ Hz. For an infinite steel plate, the Nyquist limit is however already reached at $f = 30$ Hz. The clamped boundary condition leads to an effective stiffening of the plate, but the first modes already appear around 20 Hz (section 4.1).

The results of the investigation are shown in Figures 6.1 - 6.3. Figure 6.1 contains the results of a numerical prediction with a finer patch grid of 20 cm. The results for 40 cm PTF coupling of numerical and experimental plate to the cavity can be found in 6.2 and 6.3, respectively.

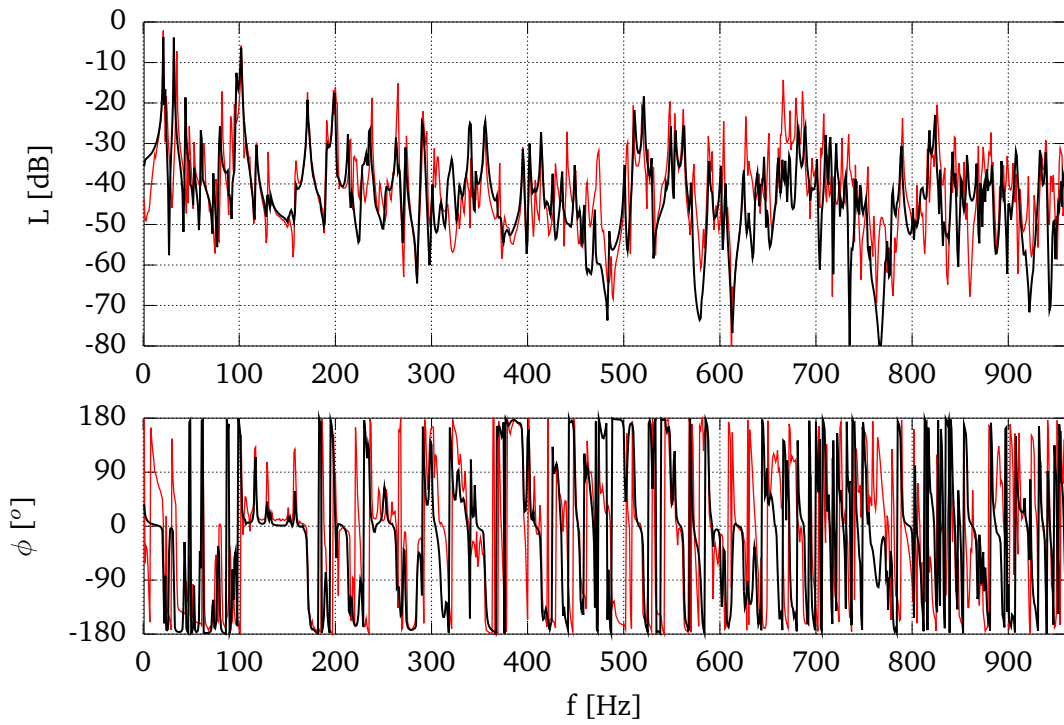


Figure 6.1: Comparison of the predicted transfer function to mic 1 with a *simulated* plate and a *simulated* cavity (black) with the reference measurement (red). (20 cm PTF)

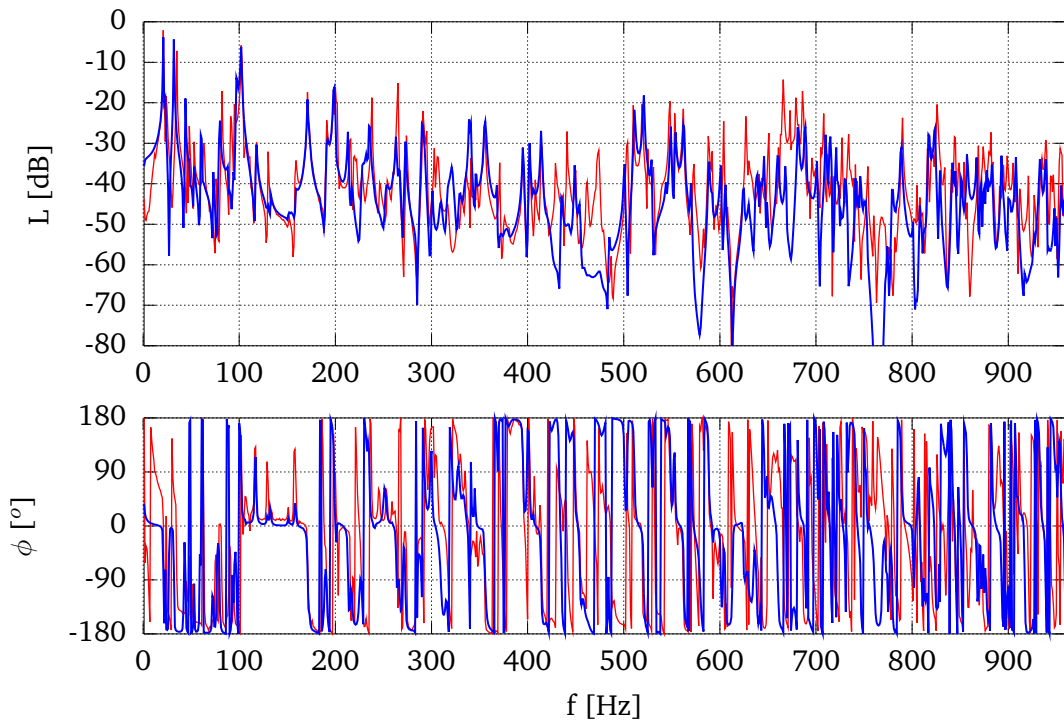


Figure 6.2: Comparison of the predicted transfer function to mic 1 with a *simulated* plate and a *simulated* cavity (blue) with the reference measurement (red). (40 cm PTF)

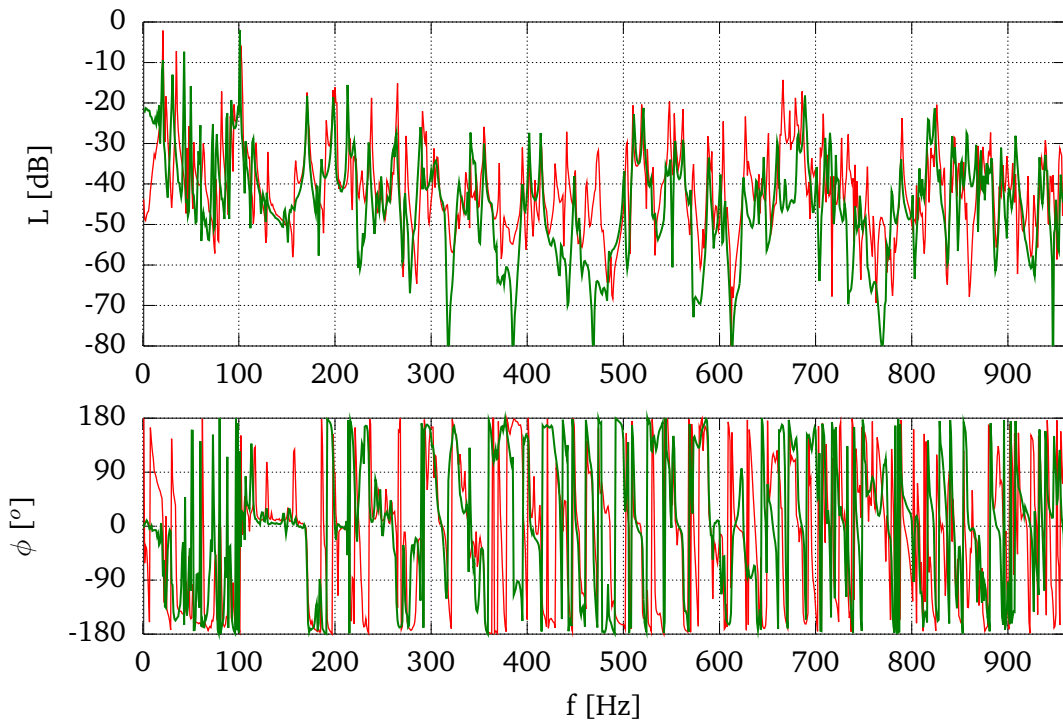


Figure 6.3: Comparison of the predicted transfer function to mic 1 with an *experimental* plate and a *simulated* cavity (green) with the reference measurement (red) at microphone position 1. (40 cm PTF)

Even with the coarse patch grid, the comparison yields good agreement with the measurements (Figs. 6.2 and 6.3) up to the $\lambda/2$ limit for the cavity rather than for the plate. This could be explained in the following way:

When plate bending waves radiate into an air cavity below the coincidence frequency, they are cancelled in the nearfield of the plate due to acoustical shortcuts. This is the case, because the wavelength in air is still much larger than the bending wavelength. The contribution to the cavity modes depends mainly on long-wave phenomena on the plate, which can be described by a coarse grid.

This can explain, why the results are still valid above the plate wavelength limit at 30 Hz. But it does not tell us, why the results of the 40 cm patches above the air limit of 430 Hz are still nearly as good as for the 20 cm patches. There is, however, another specific simplification in our test case:

The excitation of the plate has been performed on a whole 40×40 cm patch and not by a single point force. Since the propagation of short wavelengths inside the plate are canceled by the uniform excitation, the main driver for the radiation is the exciting patch. The excitation of cavity modes with a transverse wavelength smaller than 80 cm is therefore not very efficient. Thus, there is not a big difference, if the interface resolution is increased, because the excitation is still performed on a larger length scale.

6.2 Bare plate + two cavities

Before including porous damping materials, the accuracy of the method with more layers was tested. For this purpose, a virtual cut of the cavity was performed at the position of the upper surface of the porous layer. Thus, the air cavity from (6.1) is replaced by a coupled system of a thin air layer of the foam dimensions and the remaining cavity. In the ideal case, this should yield the same results as the plate-cavity system. A comparison of this plate-cavity-cavity system to the original plate-cavity system (6.1) can be found in Figure 6.4.

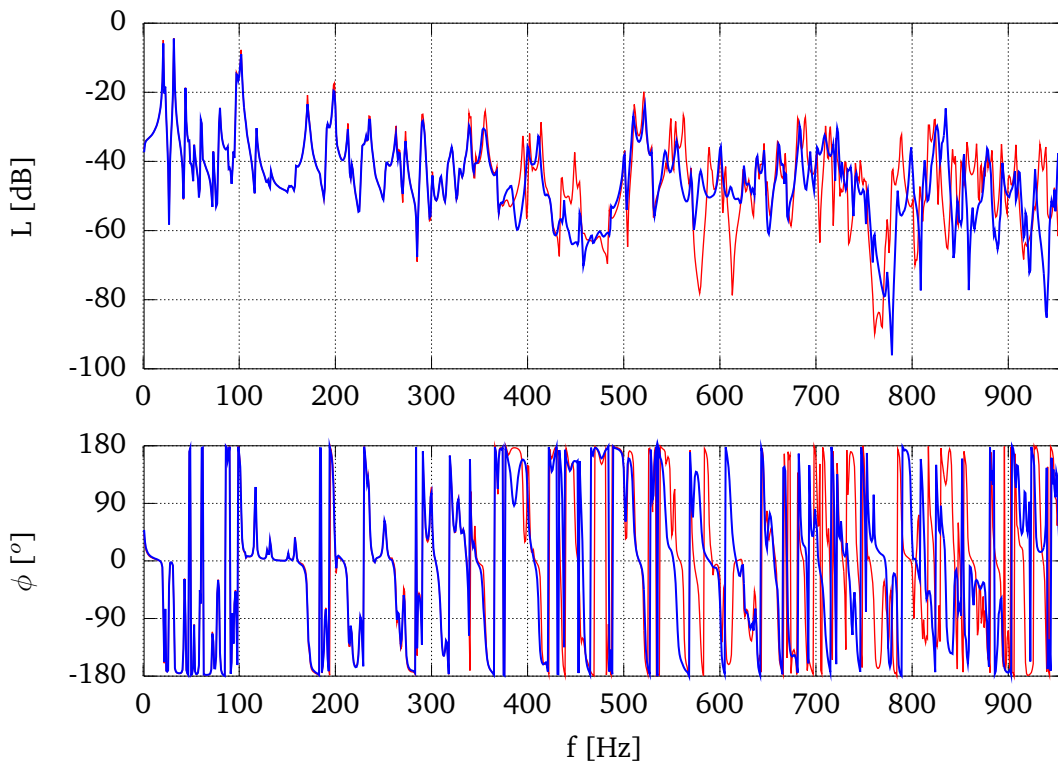


Figure 6.4: Comparison of the transfer function to mic 1 of a simulated plate coupled to two air layers (blue) and the untrimmed system 6.1 with a single air cavity (red). (40 cm PTF)

The inclusion of the additional air layer provides a very accurate reconstruction until the $\lambda/2$ limit of 400 Hz for 40 cm PTF. For higher frequencies, the method only reproduces some specific modes that are not influenced by the patch size (see section 5.2). Similar results should be expected when the thin air layer is replaced by a porous foam layer.

6.3 Plate + foam + cavity

The final test case for the coupling scheme consists of a plate, a foam layer and an air cavity (trimmed system). The foam introduces damping into the system - the resonance peaks will be lower and wider. The response to a uniform pressure excitation on plate patch no. 5 has been reconstructed by application of the PTF coupling scheme. Both numerical and experimental characterization schemes for the plate and the foam layer were considered. For the foam, the results from the indirect method (4.2.1) were used. The resulting transfer functions to a reference microphone position can be found in Figures 6.5-6.8.

All configurations yield good agreement in the valid frequency range of $f < 400$ Hz. A comparison between the average results over 1/3 octave bands is shown in Figures 6.9 and 6.11.

The simulated foam layer yields more accurate results, which may be related to uncertainties in the measurement. Especially, the errors in the third-octave band around 100 Hz, that are visible in Figure 6.11, are most likely a result of measurement noise in the characterization procedure (Figure 4.10 and 4.10). Smoothing the terms of the foam transfer matrix in the low frequency range could improve the results. The simplifications for the foam layer described in 4.2 have no negative effect, as the comparison of the numerical results in 6.9 and 6.10 shows. In the latter case, the matrix has been reduced to the quasi-two-dimensional, next-neighbor simplification as in the experimental characterization.

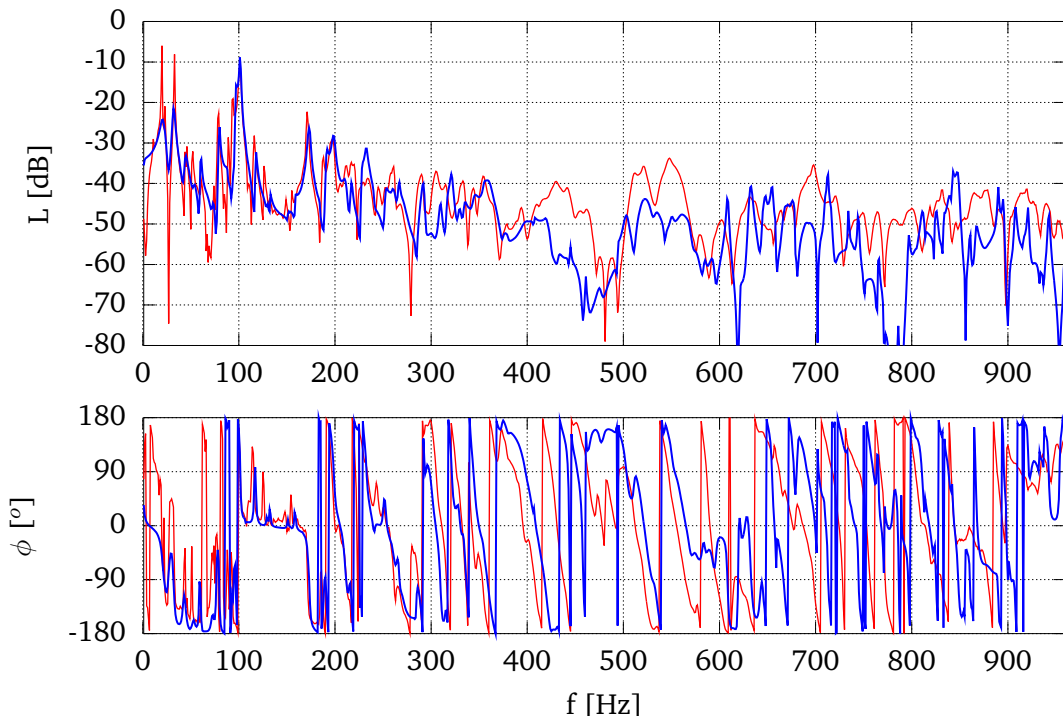


Figure 6.5: Comparison of the transfer function to mic 1 of the trimmed system with *simulated plate*, *simulated foam* and *simulated cavity* (blue) with the reference measurement (red). (40 cm PTF)

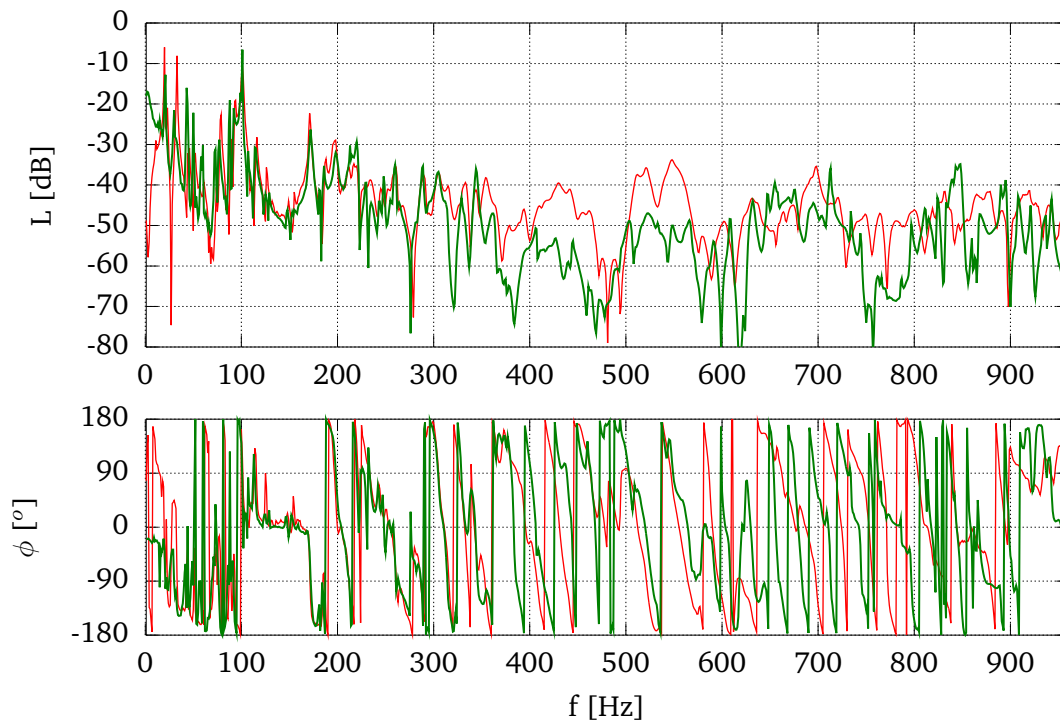


Figure 6.6: Comparison of the transfer function to mic 1 of the trimmed system with *experimental plate*, *simulated foam* and *simulated cavity* (green) with the reference measurement (red). (40 cm PTF)

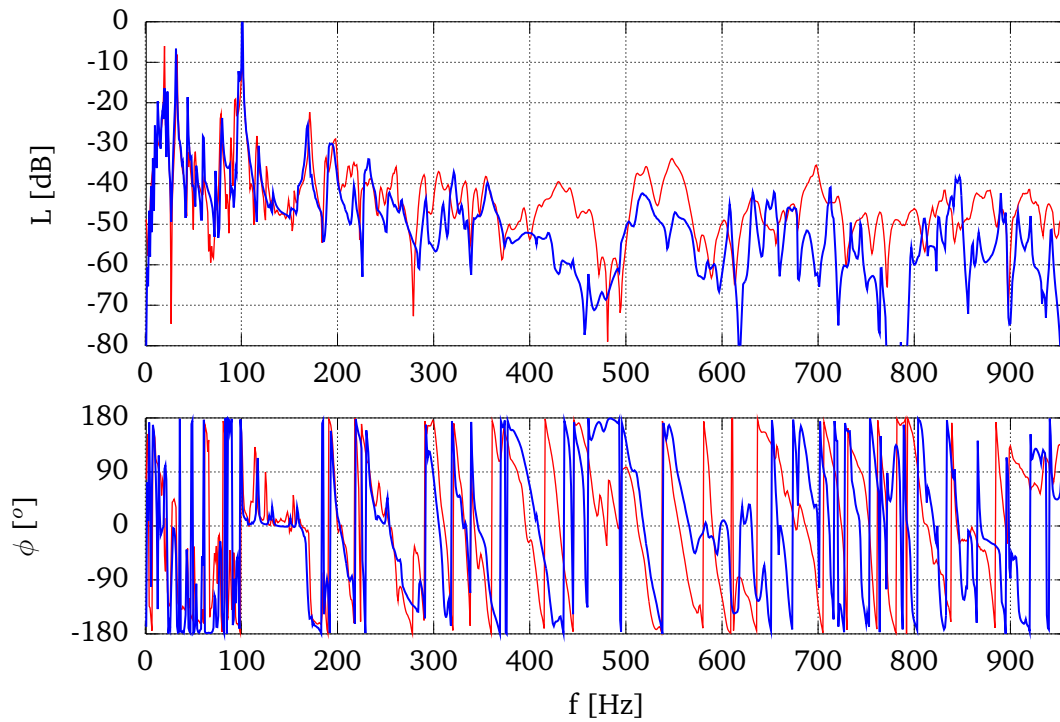


Figure 6.7: Comparison of the transfer function to mic 1 of the trimmed system with *simulated plate*, *experimental foam* and *simulated cavity* (blue) with the reference measurement (red). (40 cm PTF)

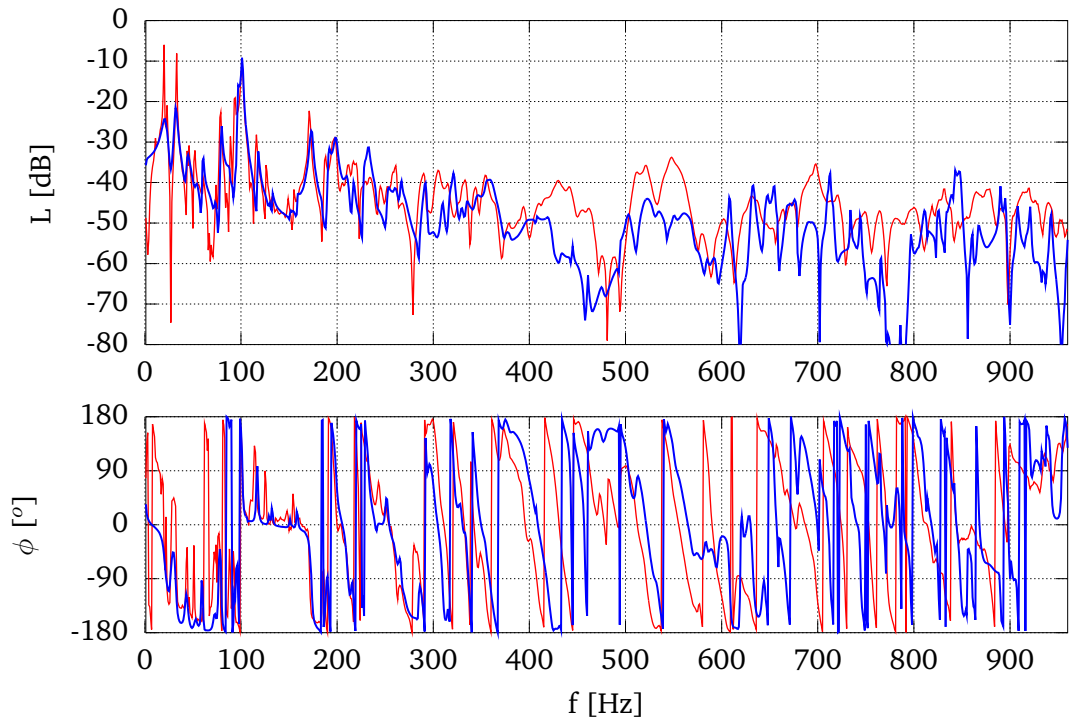


Figure 6.8: Comparison of the transfer function to mic 1 of the trimmed system with *experimental plate*, *experimental foam* and *simulated cavity* (green) with the reference measurement (red). (40 cm PTF)

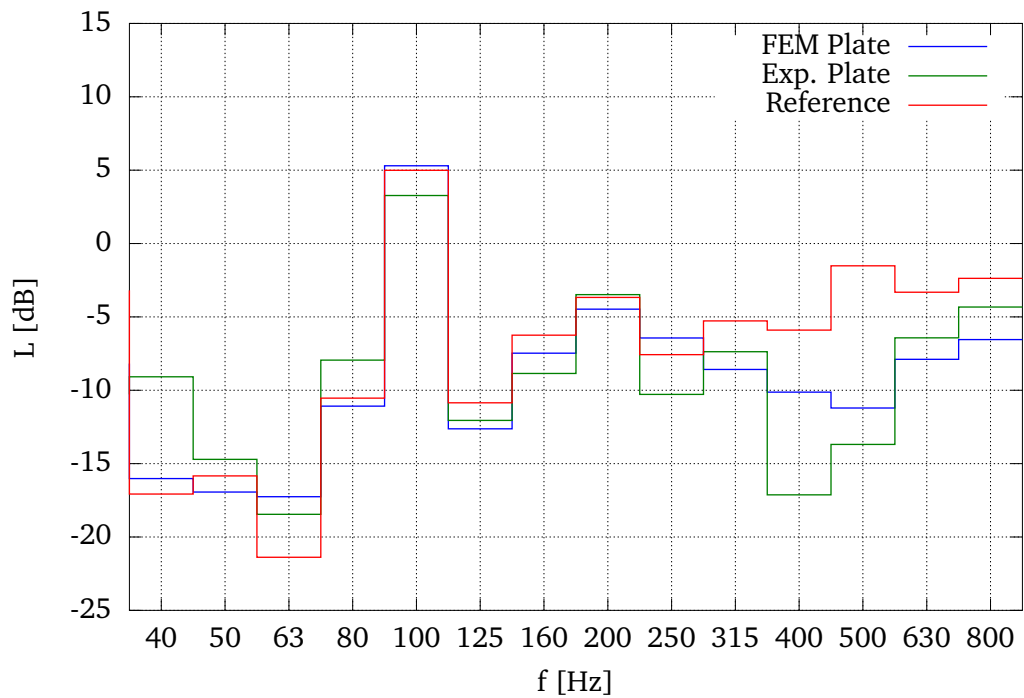


Figure 6.9: 1/3 octave band transfer function to mic 1 of the trimmed system with *simulated, full foam* compared to a reference measurement. (40 cm PTF)

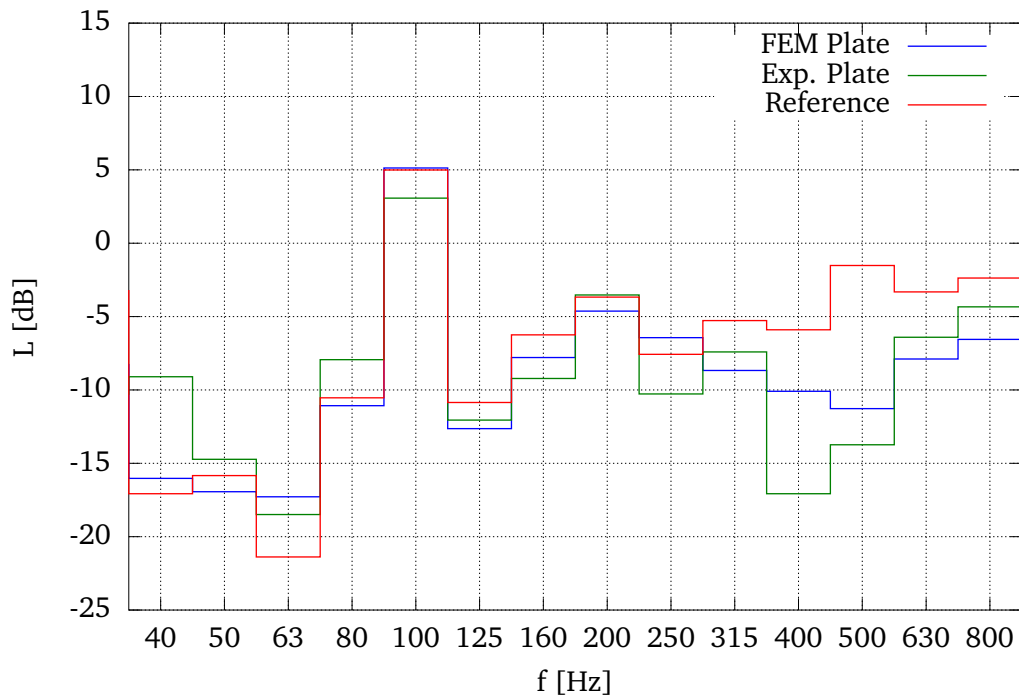


Figure 6.10: 1/3 octave band transfer function to mic 1 of the trimmed system with *simulated, reduced foam* compared to a reference measurement. (40 cm PTF)

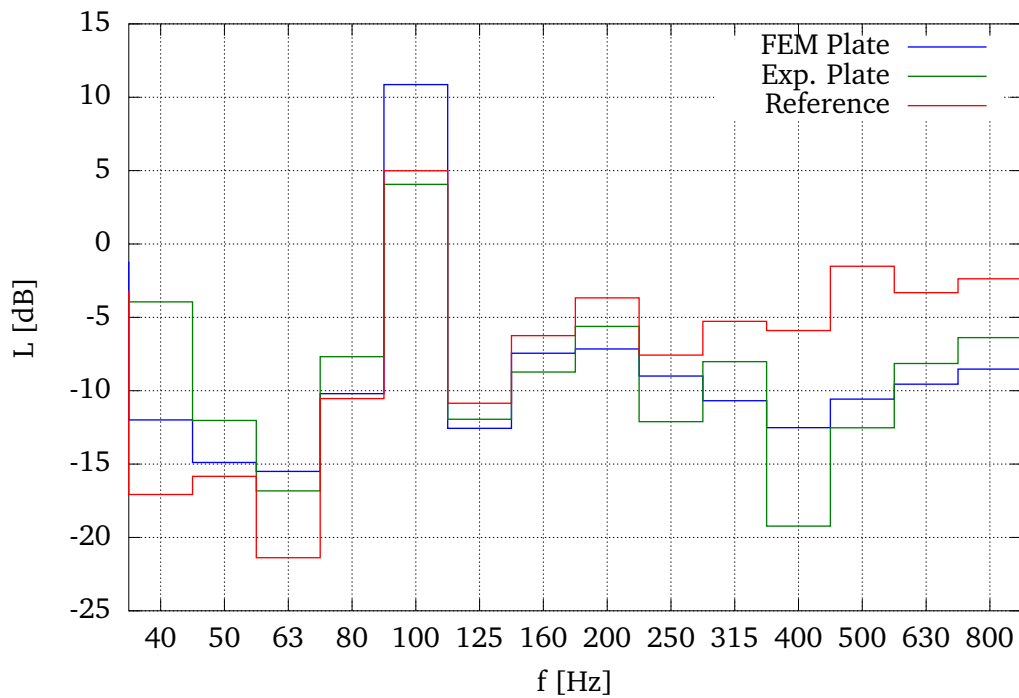


Figure 6.11: 1/3 octave band transfer function to mic 1 of the trimmed system with *experimental, reduced foam* compared to a reference measurement. (40 cm PTF)

Conclusion and Outlook

In this thesis, a hybrid method for the characterization and coupling of different vibro-acoustic components was presented. The method was applied to well-known systems that have been modeled numerically. Based on the results of these investigations, proposals for possible experimental characterization procedures were made. Experimental results based on these approaches were compared to the output of numerical models. Finally, the full system was assembled using different combinations of numerically and experimentally characterized components. The response of the coupled system was compared to the results of a validation measurement.

Even though the method yields good agreement with the validation within its frequency limits, there are still many open questions: Is the number of measurements to construct full matrices feasible in applications? Is the method suited for more complex geometries and materials? Can the accuracy and frequency range be increased by using different basis functions than homogenous patches?

However, the most important aspect of the procedure is the possibility to combine simulated and experimental results. Therefore, the goal should be to apply it to systems that lack an accurate numerical description but allow an experimental characterization of their vibro-acoustic behavior. One example for such systems is the air cavity in the interior of a car, including the whole damping treatment on non-coupling surfaces. Multi-layered trim materials pose a special challenge, since it is not yet clear how to treat the added weight to the structure and the inconsistency between impedance and mobility picture if a material consists of both a fluid and an elastic skeleton.

Appendix A

Mathematical Background

A.1 Elliptic Boundary value problems of second order

The hyperbolic wave equations that are obtained from vibroacoustic problems become elliptic when transformed to the frequency domain [Polyanin, 2002]. Consequently, their result depends solely on the boundary conditions. The most general form of the boundary value problem for a function $\mathbf{u}(\mathbf{r})$ is given by two equations with linear differential operators for the interior Ω and the boundary $\partial\Omega$,

$$\mathbf{L}\mathbf{u} = \mathbf{f} \text{ in } \Omega \quad (\text{A.1})$$

$$\mathbf{M}\mathbf{u} = \mathbf{t} \text{ on } \partial\Omega. \quad (\text{A.2})$$

The most simple (local) boundary conditions for a subsection S of $\partial\Omega$ are:

1. *Dirichlet* or *essential* boundary condition with imposed values:

$$\mathbf{u}(\mathbf{r})|_{\mathbf{r} \in S} = \mathbf{u}^S(\mathbf{r})$$

2. *Neumann* or *natural* boundary condition with imposed normal derivatives:

$$\left. \frac{\partial u_i(\mathbf{r})}{\partial n} \right|_{\mathbf{r} \in S} = w_i^S(\mathbf{r})$$

3. *Robin* or *impedance* boundary condition:

$$a_i u_i(\mathbf{r})|_{\mathbf{r} \in S} + b_i \left. \frac{\partial u_i(\mathbf{r})}{\partial n} \right|_{\mathbf{r} \in S} = c_i$$

If there are several sections with different boundary conditions of the mentioned types, they are called *mixed boundary conditions*.

A.1.1 Weak form and variational formulation

Let a function $\mathbf{u}(\mathbf{r})$ satisfy the linear partial differential equation (A.1). We apply a scalar product with an arbitrary test function $\delta\mathbf{u}(\mathbf{r})$ and integrate over the volume

inside the boundaries,

$$\int_{\Omega} [\delta \mathbf{u} \cdot \mathbf{L} \mathbf{u} - \delta \mathbf{u} \cdot \mathbf{f}] dV + \int_{\partial \Omega} [\delta \mathbf{u} \cdot \mathbf{M} \mathbf{u} - \delta \mathbf{u} \cdot \mathbf{t}] dS = 0. \quad (\text{A.3})$$

This expression is called the weak form of (A.1). Since the test function $\delta \mathbf{u}(\mathbf{r})$ can be arbitrarily chosen, it can be proven [Zienkiewicz and Taylor, 2000], that the weak form is equivalent to the original form of the equation.

A.1.2 Numerical solution using the finite element method

The finite element method (FEM) was initially used in mechanical engineering for predictions of the static and dynamic response of solid structures. Over the last 50 years it has been generalized to a general tool for solving a high number of classes of partial differential equations. The book of Zienkiewicz and Taylor [2000] provides an extensive overview over the method and its applications. In this work we limit ourselves to linear boundary value problems exclusively. The process of the numeric calculation with the commonly used Galerkin weighted residual approach consists of the following steps:

1. Discretize the equation domain to a finite mesh
2. Choose a finite set $\{\phi_i(\mathbf{r})\}$ of shape functions that are locally defined on a specific mesh element and zero otherwise. Consequently, they fulfill an orthogonality relation,

$$\int_{\Omega} \phi_i(\mathbf{r}) \phi_j(\mathbf{r}) dV = \begin{cases} 1 & (i = j) \\ 0 & (i \neq j) \end{cases}. \quad (\text{A.4})$$

3. Discretize the weak form (A.3) of the problem by approximating all terms as linear combinations of the shape functions,

$$\begin{aligned} \mathbf{u}(\mathbf{r}) &\approx \sum_{i=0}^N u_i \phi_i(\mathbf{r}) \\ \mathbf{L} \mathbf{u}(\mathbf{r}) &\approx \sum_{i=0}^N u_i \mathbf{L} \phi_i(\mathbf{r}). \end{aligned}$$

In the Galerkin approach, the shape functions ϕ_i are chosen as the test functions $\delta \mathbf{u}$.

4. Apply continuity conditions on the boundaries of adjacent elements and boundary conditions on the domain boundary.
5. Solve the resulting (weakly populated) linear system of equations.

$$K_{ij} u_j = b_i \quad (\text{A.5})$$

With reference to solid mechanics (1.7) \mathbf{K} is called the stiffness matrix of the system and the coefficients correspond to the degrees of freedom.

In this work, the open-source code FreeFEM++ [Hecht et al., 2007] has been used. It provides triangular (2D) and tetrahedral (3D) elements with polynomial shape functions of up to the 4th order and Morley elements of the first order [Morley, 1968] for plate-bending problems.

A.1.3 Schur complement system

The right side of (A.5) will be only nonzero for regions with an excitation term ($\mathbf{f} \neq 0$ in (A.1) for region 1). In the remaining region, the equations shall be homogenous. The equations will then be of the form

$$\begin{pmatrix} \mathbf{K}_{11} & \mathbf{K}_{12} \\ \mathbf{K}_{21} & \mathbf{K}_{22} \end{pmatrix} \begin{pmatrix} \mathbf{u}_1 \\ \mathbf{u}_2 \end{pmatrix} = \begin{pmatrix} \mathbf{b}_1 \\ 0 \end{pmatrix}.$$

We can eliminate the homogenous part $\mathbf{u}_2 = -\mathbf{K}_{22}^{-1}\mathbf{K}_{21}\mathbf{u}_1$ and obtain a reduced system with

$$(\mathbf{K}_{11} - \mathbf{K}_{12}\mathbf{K}_{22}^{-1}\mathbf{K}_{21}) \mathbf{u}_1 = \mathbf{b}_1. \tag{A.6}$$

This system is called the Schur complement or condensed system. If only the boundary of the domain is excited, the reduced matrix it is an approximation for the Poincaré-Steklov-Operator, that defines the whole PDE by a (strongly nonlocal) equation on the boundary [Toselli and Widlund, 2005].

List of Figures

1.1	System of a mass, a spring and a damper	6
1.2	Acoustic wavelengths in media with different speed of sound	9
1.3	Bending wavelength for steel plates of different thickness	12
2.1	Discrete approximation of the surface pressure values $p^S(\mathbf{x})$ by p_i^S	17
2.2	Coupled fluid cavities	19
2.3	Elastic plate coupled to a fluid cavity	20
2.4	Coupled plate-fluid-fluid system	21
2.5	Test problem of a rigid cavity split in halves	24
2.6	Response of two patch-coupled rigid-walled rectangular air cavities	25
3.1	Vibroacoustic test rig	26
3.2	Microphone positions inside the cavity	27
3.3	Interior of the air cavity	28
3.4	Comparison between modal superposition and FEM cavity	30
3.5	Front view of the test rig	31
4.1	Simulated approximate patch mobility	34
4.2	Comparison between simulated and measured patch mobilities	35
4.3	Mobility of the loaded plate	37
4.4	Comparison of the test trim impedance terms	39
4.5	Trim sample transfer and surface impedances	39
4.6	Direct foam characterization	40
4.7	Indirect foam characterization	41
4.8	Patch input impedance direct	42
4.9	Patch transfer impedance direct	42
4.10	Patch input impedance indirect	43
4.11	Patch transfer impedance indirect	43
5.1	System of two springs	44
5.2	Patch impedance ratio	46
5.3	Patch size limit	47

5.4 Patch size effects	48
6.1 Untrimmed PTF and measurement (20 cm PTF, simulated plate) . . .	50
6.2 Untrimmed PTF and measurement (40 cm PTF, simulated plate) . . .	50
6.3 Untrimmed PTF and measurement (40 cm PTF, experimental plate) .	51
6.4 Untrimmed PTF with two air layers (40 cm PTF, sim. plate)	52
6.5 Trimmed PTF and measurement (40 cm PTF, sim. plate, sim. foam) .	53
6.6 Trimmed PTF and measurement (40 cm PTF, exp. plate, sim. foam) .	54
6.7 Trimmed PTF and measurement (40 cm PTF, sim. plate, exp. foam) .	54
6.8 Trimmed PTF and measurement (40 cm PTF, exp. plate, exp. foam) .	55
6.9 Third octave band average with simulated full foam	55
6.10 Third octave band average with simulated full foam	56
6.11 Third octave band average with experimental simplified foam	56

Bibliography

- J. Allard and N. Atalla. *Propagation of Sound in Porous Media: Modelling Sound Absorbing Materials*. John Wiley & Sons, Ltd, 2009.
- J. Allard, R. Bourdier, and C. Depollier. Biot waves in layered media. *Journal of applied physics*, 60(6):1926–1929, 1986.
- N. Atalla, R. Panneton, and P. Debergue. A mixed displacement-pressure formulation for poroelastic materials. *The Journal of the Acoustical Society of America*, 104: 1444, 1998.
- M. Aucejo, L. Maxit, N. Totaro, and J. Guyader. Convergence acceleration using the residual shape technique when solving structure-acoustic coupling with the patch transfer functions method. *Computers & Structures*, 88(11-12):728 – 736, 2010.
- M. Biot. General theory of three-dimensional consolidation. *Journal of applied physics*, 12(2):155–164, 1941.
- M. Biot. Theory of propagation of elastic waves in a fluid-saturated porous solid. i. low-frequency range. *The Journal of the Acoustical Society of America*, 28:168, 1956.
- Y. I. Bobrovnikskii. A theorem on the representation of the field of forced vibrations of a composite elastic system. *Acoustical Physics*, 47:507–510, 2001.
- I. Bork. Report on the 3rd round robin on room acoustical computer simulation part ii: Calculations. *Acta Acustica united with Acustica*, 91(4):753–763, 2005.
- J. Chazot and J. Guyader. Prediction of transmission loss of double panels with a patch-mobility method. *Journal of the Acoustical Society of America*, 121:267–278, 2007.
- R. Ciskowski and C. Brebbia. *Boundary element methods in acoustics*. Springer, 1991.
- H. de Bree, P. Leussink, T. Korthorst, H. Jansen, T. Lammerink, and M. Elwenspoek. The μ -flown: a novel device for measuring acoustic flows. *Sensors and Actuators A: Physical*, 54(1):552–557, 1996.
- M. Delany and E. Bazley. Acoustical properties of fibrous absorbent materials. *Applied acoustics*, 3(2):105–116, 1970.

- F. Fahy. Statistical energy analysis: a critical overview. *Philosophical Transactions of the Royal Society of London. Series A: Physical and Engineering Sciences*, 346 (1681):431–447, 1994.
- F. Fahy. *Foundations of Engineering Acoustics*. Academic Press, 2001.
- F. Hecht, O. Pironneau, A. Le Hyaric, and K. Ohtsuka. Freefem++. *Laboratoire JL Lions, University of Paris VI, France*, 70, 2007. URL <http://www.freefem.org/>.
- A. Krokstad, S. Strom, and S. Sørsdal. Calculating the acoustical room response by the use of a ray tracing technique. *Journal of Sound and Vibration*, 8(1):118–125, 1968.
- N. Lalor and H. Pribsch. The prediction of low-and mid-frequency internal road vehicle noise: a literature survey. *Proceedings of the Institution of Mechanical Engineers, Part D: Journal of Automobile Engineering*, 221(3):245–269, 2007.
- L. Landau and E. Lifshitz. *Theory of Elasticity*, volume 7 of *Course of Theoretical Physics*. Pergamon Press, 1986.
- L. Landau and E. Lifshitz. *Fluid Mechanics*, volume 6 of *Course of Theoretical Physics*. Pergamon Press, 1987.
- R. Lyon. *Statistical energy analysis of dynamical systems: theory and applications*. 1975.
- L. Morley. The triangular equilibrium element in the solution of plate bending problems. *Aero. Quart*, 19:149–169, 1968.
- P. Morse and K. Ingard. *Theoretical acoustics*. Princeton Univ Pr, 1986.
- E. Nijman, J. Rejlek, G. Veronesi, and C. Albert. K2 - Intermediate Report ViF-ZB-C04T04/2012. Technical report, 2012.
- M. Ouisse, L. Maxit, C. Cacciolati, and J. Guyader. Patch transfer functions as a tool to couple linear acoustic problems. *Journal of Vibration and Acoustics*, 127: 458–66, October 2005.
- R. Panneton and X. Olny. Acoustical determination of the parameters governing viscous dissipation in porous media. *The Journal of the Acoustical Society of America*, 119:2027, 2006.
- G. Pavic. Air-borne sound source characterization by patch impedance coupling approach. *Journal of Sound and Vibration*, 329(23):4907 – 4921, 2010.
- A. Polyanin. *Handbook of linear partial differential equations for engineers and scientists*. CRC Press, 2002.
- S. Pride, F. Morgan, and A. Gangi. Drag forces of porous-medium acoustics. *Physical review B*, 47(9):4964, 1993.

- R. Rannacher. On nonconforming and mixed finite element methods for plate bending problems: The linear case. *RAIRO*, 13:369–387, 1979.
- A. Toselli and O. Widlund. *Domain decomposition methods—algorithms and theory*, volume 34. Springer Verlag, 2005.
- O. C. Zienkiewicz and R. L. Taylor. *The finite element method: The Basis*, volume 1. Butterworth and Heinemann, 5 edition, 2000.